5-2011

# Coanda-Assisted Spray Manipulation Implementation to Plasma Spray

Katie E. Mabey
*Utah State University*

# COANDA-ASSISTED SPRAY MANIPULATION IMPLEMENTATION TO PLASMA SPRAY

by

Katie E. Mabey

A thesis submitted in partial fulfillment
of the requirements for the degree

of

MASTER OF SCIENCE

in

Mechanical Engineering

Approved:

| | |
|---|---|
| Dr. Barton Smith<br>Major Professor | Dr. Robert Spall<br>Committee Member |
| Dr. Christine Hailey<br>Committee Member | Dr. Byron Burnham<br>Dean of Graduate Studies |

UTAH STATE UNIVERSITY
Logan, Utah

2011

# Abstract

Coanda-Assisted Spray Manipulation Implementation to Plasma Spray

by

Katie E. Mabey, Master of Science

Utah State University, 2011

Major Professor: Dr. Barton Smith
Department: Mechanical and Aerospace Engineering

Coanda-assisted Spray Manipulation (CSM) is a means of modifying the direction of a jet. Previous isothermal static vectoring research is expanded to plasma spray. Two-dimensional Particle Image Velocimetry (PIV) was used to determine the vectoring results for small angles between 5-10°. Suitable parameters were determined for use on a plasma spray gun for small angle vectoring. Three-dimensional PIV was used to determine the effect of high speed rotation on a vectored jet. A 2-piece CSM collar was retrofitted to a Praxair SG-100 plasma spray gun that replaced the standard faceplate. Two separate collars were tested: one designed for small vector angles and one for larger vector angles. The small-angle device could modify the trajectory of zirconia powder up to several degrees. Doing so could realign the plasma with the powder, resulting in increased powder temperature and velocity. The large-angle device could vector the plasma jet up to 45°; however the powder did not vector as much. Under large-angle vectoring, the powder velocity and temperature decreased steadily with vector angle. Both devices were tested using a supersonic configuration.

(84 pages)

Thank you to my adviser, Dr. Smith, for teaching and guiding me, to my brother Ben for making me want to be an engineer, and most of all to my husband Josh for keeping me sane and making me laugh.

# Contents

# List of Tables

# List of Figures

# Nomenclature

| | |
|---|---|
| $\nu$ | Kinematic viscosity |
| $\omega$ | Rotation rate of vectored jet |
| $\rho$ | Density |
| $\rho_c$ | Density of the control jet |
| $\rho_p$ | Density of the primary jet |
| $\tau$ | Time constant for the jet |
| $\theta$ | Vector angle around Coanda surface |
| $a$ | Radius of curvature of Coanda surface |
| $A_c$ | Cross-sectional area of the control jet exit |
| $A_p$ | Cross-sectional area of the primary jet exit |
| $b$ | Slot width for flow around Coanda surface |
| $D$ | Diameter of the primary jet exit |
| $j$ | Distance from the control jet to the tangential center fo the Coanda surface (location of jet impingement) |
| $J^*$ | Momentum flux ratio $J_c/J_p$ |
| $J_c$ | Momentum flux fo the control jet |
| $J_p$ | Momentum flux of the primary jet |
| $P$ | Supply pressure of the jet |
| $p_\infty$ | Ambient pressure |
| $p_s$ | Pressure on the wall of the Coanda surface |
| $P_x$ | Paralell component of particle momentum |
| $P_y$ | Perpendicular component of particle momentum |
| $q$ | Jet volume flow ratio as defined by Juvet [5] |
| $Q_c$ | Volume flow rate of the control jet |
| $Q_p$ | Volume flow rate of the primary jet |
| $t$ | Time per revolution for rotating vectored jet |
| $u$ | Mean velocity of the primary jet |

# Chapter 1

# Introduction

This thesis seeks to apply Coanda-Assisted Spray Manipulation (CSM) to plasma sprays. CSM has been developed as a flow control method using the Coanda effect. The Coanda effect is the tendency of a jet near a curved surface to follow that curved surface. CSM utilizes a high momentum control jet near a curved surface to manipulate a high flow rate primary jet through entrainment. If the high momentum flow, hereafter called secondary or control flow, is sufficiently close to a curved surface, the secondary flow will attach to the curved surface. The trajectory of the secondary flow is modified from a straight path exiting perpendicular to the exit cross section to curved around the coanda surface and detaching from the curved surface at an angle measured from the axis of the primary flow. The primary flow, when entrained, will be pulled into a vectored trajectory by the secondary flow, so long as the secondary flow has high enough momentum flux relative to the primary flow momentum flux. This method may be applied to any primary jet given sufficient secondary momentum flux, however for this research the target application is plasma spray spray.

Plasma spray is a thermal spray method that uses plasma as a heat source to melt fine particles and propel the material toward a surface. Plasma spray temperatures are typically greater than 8000 K, which either melts or partially melts the particles. The melted or partially melted particles splat onto the substrate surface and agglomerate to form a coating. Plasma spray coatings are typically high value-added coatings applied to surfaces to provide resistance to heat, wear, erosion and/or corrosion protection. They may also be used to finely tune a unique set of surface characteristics [1].

Application of the CSM to plasma spray has been proposed as a solution to three main problems. First, CSM may be used to manipulate the angle of the plasma and particles

relative to the gun. It has been shown by Berndt and Leigh [2] that spray angles (measured as the angle between the substrate surface and the axis of the spray device) less than 90° produce inferior coating properties. For this reason, it is important to maintain a constant perpendicular angle to the substrate when spraying. However, this becomes difficult when the substrate is not flat. Substrate three-dimensionality is significant for many applications. For these applications, either the part or the spray must be rotated or moved to maintain the perpendicular spray angle.

Due to the high temperatures associated with plasma near the process nozzles, mechanical vectoring of the nozzle is not feasible because it would require moving parts in or near the flow. As an alternative to flow control methods of vectoring, thermal spray companies have developed gun extensions that modify the trajectory of the coating material. These gun extensions vector the flow to a fixed angle referenced to the gun. They can be cumbersome, however. In addition to vectoring the coating material and plume, the gun itself may be rotated to produce an angled spray. This may be accomplished through a robotic arm device that can be programmed to rotate the gun relative to the sprayed surface. Robotic arms may be costly to acquire and operate and require complex programming. CSM could potentially allow the plasma and spray particles to be vectored in real time to maintain perpendicular spray for three-dimensional parts.

The second plasma spray application of CSM is to realign the plasma with the injected particles. For plasma spray, the particles must be injected into the plasma plume from a reservoir. This is done perpendicular to the direction of the plasma jet in about 90% of plasma spray guns. This perpendicular injection occurs very near the exit of the the device or after the exit of the device, which does not allow sufficient stream-wise length for the particles to fully change direction. This results in the particles and plasma leaving the thermal spray device at an angle compared to the direction of the gun. The angle of the particles is generally higher than the angle of the plasma, so the particles leave the plasma jet at some point, thus resulting in lower particle temperature and velocity. Lower particle temperatures can cause adverse changes to coating properties and a reduction in

deposition efficiency (percentage of sprayed material that adheres to the substrate). A possible application of the CSM would be to vector the plasma plume in the direction of the particles leaving the plume to realign the plume with the particle trajectory.

An final use of CSM to thermal sprays is in heat management. Often, the substrate that is being sprayed becomes very hot and the part may warp or melt. A possible use of CSM would be to vector the plasma away from the trajectory of the particles to reduce substrate heating or manage heating of the particles.

A previous study by Allen and Smith [3] considered isothermal, subsonic flow controlled by a CSM device. The study was a fundamental look at CSM and the relevant parameters for isothermal, stationary, subsonic flow. It determined effects of device geometry to the performance and maximum vector angle that is possible for the device, the relevant parameter that determines the vector angle, and the effects of vectoring on the primary jet. This paper was an introductory study that did not look at application of the CSM to plasma sprays. In order to use a CSM device for this application, additional information is needed. This study will investigate CSM behavior in the small angle region (5-10$^{o}$) for use in the plasma/particle realignment application and the jet response and distortion when rotated at high rotation rates for dynamic vectoring applications. Finally, a design for a commercially available plasma spray gun will be proposed and the design will be used for a vectored plasma spray study.

# Chapter 2

# Literature Review

This research focuses on applying a CSM device to plasma spray. A brief discussion of the research done on the fluid dynamic aspects of the Coanda effect that are utilized by the CSM device will be given as well as a summary of the previous study done on CSM. Additionally, literature on the three main plasma spray applications of the CSM will be presented, namely off-angle spraying, particle injection realignment, and substrate thermal management.

## 2.1 Coanda Effect and CSM

### 2.1.1 Coanda Effect and Parallel Jet Mixing

Although there are three different phenomena that are associated with the term Coanda, for the purposes of this paper, the Coanda effect will be defined as the tendency of a jet initially tangent to a curved surface to attach to that curved surface. Another definition that is also useful is the tendency of jet flows over a convex surface to entrain ambient fluid and increase more rapidly than that of a plane wall jet. A fundamental study performed by Newman [4] sought to explain this phenomena and investigate the relevant parameters for two-dimensional flow around a circular cylinder as shown in Fig. 2.1 with cylinder radius $a$, jet slot width $b$, and attachment angle $\theta$.

The Coanda effect works through a balance of pressures and centrifugal forces. The pressure near the surface of the cylinder is less than that of the surroundings which causes the flow to attach to the curved surface and to entrain more flow from the surroundings. As the attached jet entrains ambient fluid, the velocity of the jet decreases, therefore the pressure along the surface of the cylinder increases forming an adverse pressure gradient.

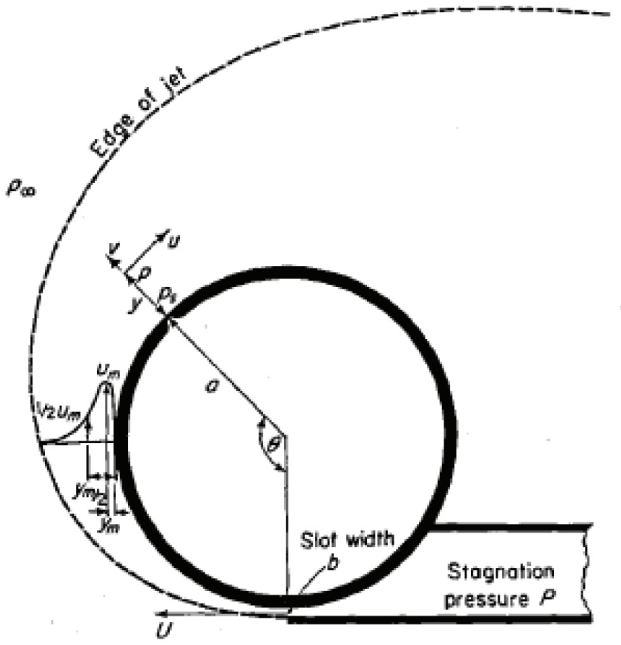


FIG. 6. Flow of a two-dimensional jet round a circular cylinder.

Fig. 2.1: Two-dimensional flow around a cylinder as used by Newman [4].

The flow remains attached until the pressure on the surface is equal to the ambient pressure $p_\infty$ when the flow separates from the wall.

The Reynolds number for the jet was calculated as

$$Re = \left[\frac{(P - p_\infty)ba}{\rho\nu^2}\right]^{1/2} \tag{2.1}$$

where $P$ is the supply pressure of the jet, $\rho$ is the density of the jet, and $\nu$ is the kinematic viscosity of the jet. The separation angle around the cylinder was found to be a function of the Reynolds number. Newman determined that for $Re > 4 * 10^4$ the separation angle was constant. An equation was proposed by Newman for separation angle

$$\theta_{sep} = 245 - 391\frac{\frac{b}{a}}{1 + \frac{9}{8}\frac{b}{a}}. \tag{2.2}$$

The Coanda effect was applied to a parallel jet situation by Juvet [5] similar to Allen and Smith [3]. The device used by Juvet was axisymmetric, using a circumferential slot

to blow air around an annulus shaped collar with a curved inner surface. Also, the device used two flows, a primary round jet in the center and a control jet exiting tangential to the curved collar.

The study by Juvet used constant geometry with varied jet volume flow ratio, defined as

$$q = \frac{Q_c}{Q_p} \tag{2.3}$$

where $Q_c$ is the wall jet volume flow rate and $Q_p$ is the primary jet volume flow rate. This parameter varied from 0-0.15. Juvet identified a subcritical blowing range for $q < 0.10$, where the primary jet remains jet-like but is widened significantly and the center-line velocity decreased due to entrainment. A supercritical blowing range was also identified for $q > 0.10$, where the primary jet becomes a wall jet attached to the Coanda collar and remains attached for the full extent of the collar. As the flow ratio increased, the vectoring increased as identified by the center-line velocity decreasing to zero.

### 2.1.2 Coanda-Assisted Spray Manipulation

A fundamental study on Coanda-assisted Spray Manipulation was performed by Allen and Smith [3]. The study used an experimental test CSM that accommodated several control slot sizes, Coanda surface curvatures, and three secondary jet impingement locations. It was determined that the relevant parameter to control vector angle was the ratio of the momentum flux of the control flow to the primary flow, defined as

$$J^* = J_c/J_p = \frac{\rho_c Q_c^2}{A_c} / \frac{\rho_p Q_p^2}{A_p} \tag{2.4}$$

where $J_c$ is the momentum flux of the control jet; $J_p$ is the momentum flux of the primary jet; $\rho_c$, $Q_c$, and $A_c$ are the density, volume flow rate, and exit cross-sectional area of the control jet; and $\rho_p$, $Q_p$, and $A_p$ are the density, volume flow rate, and exit cross-sectional area of the primary jet. The relationship between momentum flux ratio and vector angle

was considered for the various geometries.

The test CSM device was used with various permutations of the geometric variables to determine the effect of each. The jet impingement location $j$ is defined as the location downstream from the jet exit that the coanda surface begins to curve away from the center. This was varied independently of the other geometric variables and it was determined that the optimum of the three jet impingement locations was $j/D = 1.00$ where $D$ is the diameter of the primary jet exit. This produced a larger maximum vector angle than the $j/D = 0.00$ location. The furthest jet impingement location tested was $j/D = 2.00$ which produced the largest vector angle with the smallest momentum flux ratio, however the primary jet experienced undesirable spreading. The rest of the geometric variables are varied independently of jet impingement location, with $j/D = 1.00$ for all tests.

The vector angle for various control slot sizes and coanda surface curvatures was measured. The results are shown in Fig. 2.2. From the figure, it is observed that the larger the control slot is, the higher the maximum vector angle is and the smaller the momentum flux ratio is required to reach the maximum vector angle. It can also be seen that the larger the coanda surface curvature is, the higher the vector angle is for a given momentum flux ratio, however this trend is most apparent for smaller control slot sizes, and nearly negligible for larger control slot sizes. The 29.5% control slot was determined to be the optimum for desired large vector angles. From Fig. 2.2, it can be seen that there is a linear region where vector angle is linear with respect to $J^*$ on a semi-log plot. This is important for many applications to be able to predict behavior between data points.

Spreading of the control jet was measured comparing the vectored jet cross sectional area to the unvectored jet cross sectional area at $8D$ and $12D$ downstream of the jet exit. A plot of the nondimensionalized area versus vector angle is shown in Fig. 2.3. For the case of $a/D = 5.25$ and 29.5% control slot size, there is a range of vector angles that the area ratio is nearly 1, meaning that the jet is virtually unchanged. This is desirable for the plasma spray application because spreading of the plasma would cause undesirable cooling and spreading of the particles would reduce deposition efficiency.

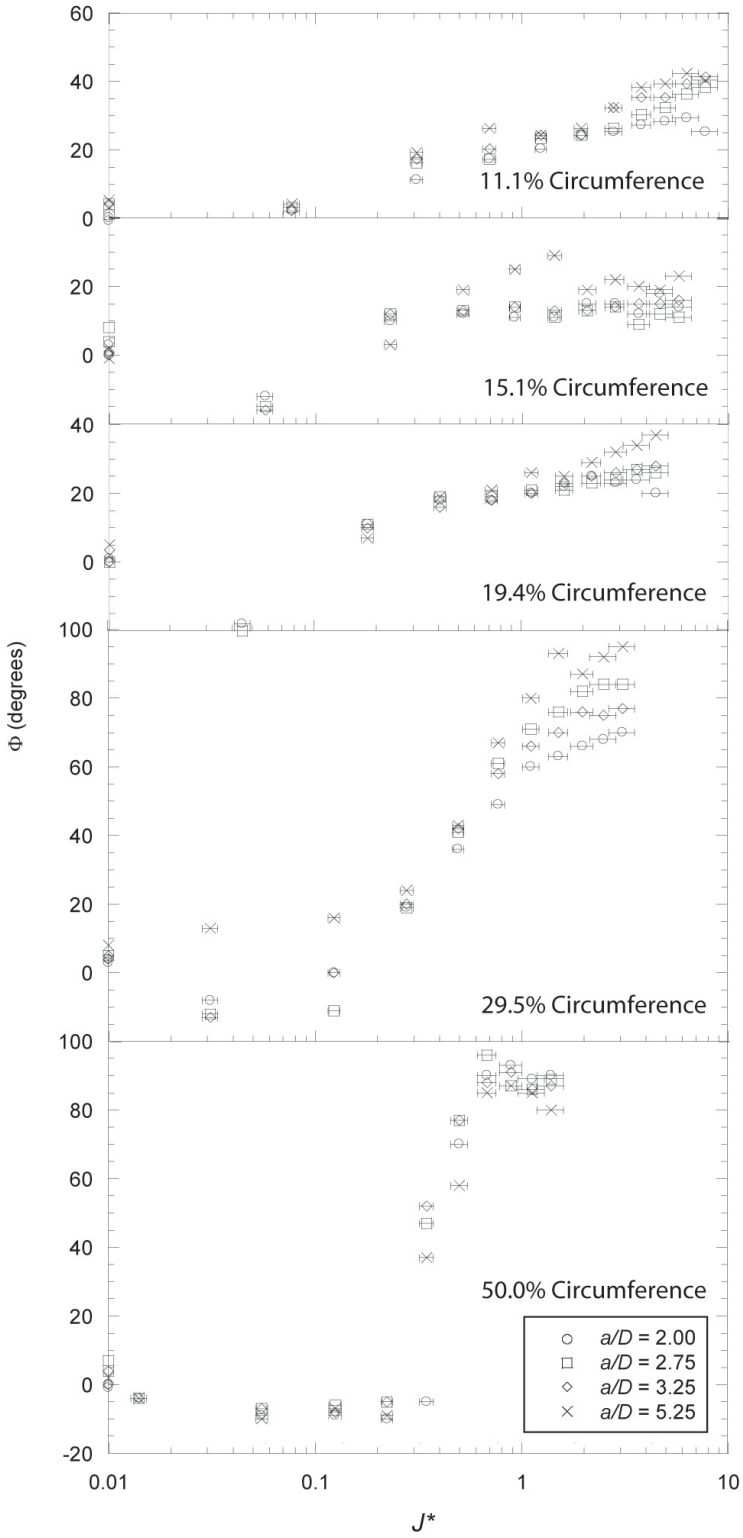


Fig. 2.2: Vector angle versus momentum flux ratio for various CSM geometries from the study by Allen and Smith [3].

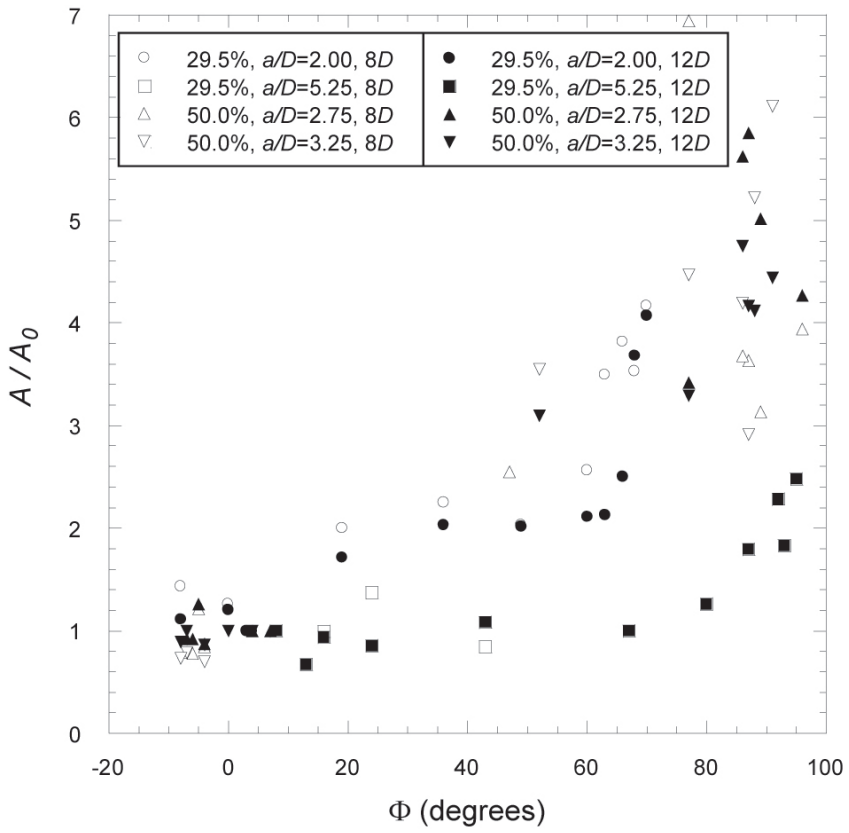


Fig. 2.3: Area of the vectored jet nondimensionalized by the area of the unvectored jet versus vector angle for 8D and 12D downstream from the jet exit from [3].

## 2.2 Off-Angle Spraying

Several studies have been performed to determine the effects of off-angle spraying [2, 6–15]. The spray angle is defined as the angle between the substrate and the axis of the spray gun, which is ideally 90º. Differences in coating properties with changing spray angle is attributed to the separation of particle velocity into parallel and perpendicular components [2, 9]. The $P_y$ component of particle momentum (perpendicular to the substrate) is called the "impacting" momentum, while the $P_x$ component (parallel to the substrate) is called the "spreading" momentum. For spray angles less than 90º, the $P_y$ component is decreased. An asymmetrical splat shape is caused by the $P_x$ component by promoting spreading away from the point of impact. According to Bussman *et al* [7], greater than 90% of the material accumulates downstream of the point of impact for small vector angles, however the area of the splat remains relatively unchanged. "Shadowing," or splat inability to cover a rough surface or previously deposited material, can occur at small angles. Adverse coating properties may also be caused by the change in spray distance across the width of the spray pattern for small spray angles. Particles at the edge of the spray pattern can experience improper melting or resolidification for small spray angles, causing reduced deposition efficiency and increased porosity.

Depending on the material that is sprayed, the effect of spray angle can change. Leigh and Berndt [2] performed tests with $NiAl$ and $Cr_3C_2 - NiCr$ sprayed onto steel at spray angles between 50º and 90º. They found that the porosity of the coating increased from 2.1 to 4.5% for $Cr_3C_2 - NiCr$ and from 2.5 to 4.2% for $NiAl$ when the spray angle was decreased from 90º to 50º. Spray angles less than 80º produced larger pores, which occurs because of the shadowing. The hardness of the coatings decreased with decreasing spray angle by about 9% for both materials. The adhesion strength decreased by 5% for $NiAl$ and 20% for $Cr_3C_2 - NiCr$ with spray angle decreased from 90º to 50º.

Experiments by Hasui *et al.* [8] determined that the coating properties of molybdenum and alumina sprayed particles had relatively little change with spray angle. The porosity of the coatings increased from 14% to 16% for molybdenum and 19% to 22% for alumina

with spray angle decrease from $90^{o}$ to $45^{o}$. This increase was declared insignificant and the coatings sprayed at small angles were not so inferior. The tensile strength of the coatings was actually found to increase with decreasing spray angle, from 1.1 $kg/mm^2$ to $2.1kg/mm^2$ for molybdenum and from 0.7 $kg/mm^2$ to 1.2 $kg/mm^2$ for alumina spayed at $90^{o}$ and $45^{o}$. The deposition efficiency decreased with decreasing spray angle from 65% to 55% for molybdenum and 75% to 65% for alumina sprayed at $90^{o}$ and $45^{o}$, but this difference was declared to be small.

For High Velocity Oxygen Fuel (HVOF) sprayed $WC-Co$ and $Cr_3C_2-NiCr$ coatings, the porosity of coatings for spray angles between $30^{o}$ and $90^{o}$ was found by Houdkova *et al.* [9] to be unaffected. This is possibly due to the high velocities associated with HVOF coatings, which could lead to more elongation and spreading of splats leading to better coating uniformity. It is important to note that though there was no difference in porosity for the coating sprayed at $30^{o}$ compared to $90^{o}$, the microstructure showed different splat shapes corresponding to the movement of the gun for different passes. When the substrate moved away from the gun, the coating had low porosity and uniformly distributed carbides. However, when the substrate was moving towards the gun, the coating had a low amount of carbides. The coatings did not show a significant decrease in hardness or surface roughness. The deposition efficiency was found to vary strongly with decreasing spray angle, from about 40% at $90^{o}$ to about 20% at $30^{o}$ for both materials.

Ilavsky *et al.* [10] analyzed coatings of alumina for porosity by various methods. Using X-ray diffraction, Mercury Intrusion Porosimetry (MIP), and the Archimedes porosimetry, the porosity was measured for spray angles ranging from $90^{o}$ to $30^{o}$. By both the MIP and Archimedes methods, the percentage of porosity was found to more than double for spray angles of $30^{o}$ compared to $90^{o}$. X-ray diffraction indicated that there was a significant change in the proportion of $\alpha - Al_2O_3$ with spray angle, indicating that there were changes in the rate of feedstock melting and solidification with changes in spray angle. Examination of the sprayed coatings indicated that the orientation of interlamellar pores does not change with spray angle, however the orientation of interlamellar cracks did change. The cracks tended to

tilt toward the spray direction. Microcrack distribution can greatly affect the survivability of sprayed coatings, and therefore the spray angle may affect the coating survivability.

### 2.3 Powder Injection Alignment

According to Fauchais [1], 90% of plasma spray guns inject the powder to be sprayed orthogonally, and because of that orthogonal injection, some of the injected particles will not enter the plasma plume and some particles will cross the plasma jet and exit the plume too quickly. Ang *et al.* [16] showed that carrier gas flow rate effects the melting state of the particles. They developed a process control chart that could be used to determine the optimum carrier gas flow rate to minimize unmelted and evaporated particles. The amount of particles that bypass the plasma jet increases with radial distance of the injector tip from the axis if the plasma jet. However, if the injector tip is too close to the plasma, clogging or melting may occur.

A basic study on three different particle injection methods was conducted by An and Gao [17]. The three different configurations they studied were axial particle injection from the cathode tip, radial injection just downstream of the anode arc root, and radial injection at the nozzle exit.

Typically, injecting the particles at the nozzle exit is the most common. It is the easiest to design and implement because the powder injection is separate from the gun and it allows the operator to see the particle trajectory and adjust the carrier gas flow rate accordingly. This method of particle injection causes added entrainment of cold air into the plasma jet which causes the plasma to cool rapidly. This adversely effects the deposition efficiency and requires higher power to sufficiently melt the particles. Additionally, internal injection of particles can produce a high deflection of the plasma jet for carrier gas mass flow rates greater than 10% of the plasma gas mass flow rate [18].

Injecting the particles just downstream of the anode arc root is advantageous compared to injecting the particles at the nozzle exit. The temperature and velocity at the injection point is much higher, therefore more energy may be transferred to the particles. The containment of the gun will reduce particle scatter and increase deposition efficiency. This

injection method, however, is prone to depositing particles on the nozzle wall and may cause choking of the jet or clogging of the particle feed lines. Additionally, the thermophoretic force generated by the radial temperature gradient in the plasma plume causes most of the particles to only reach the edge of the plume and very few reach the center, thus reducing heating of the particles. The carrier gas and particle injection has little effect on the plasma plume for external injection [18].

In the study by An and Gao [17], a single plasma spray device was used to test all three injection methods. The study found that the melting of the particles with axial injection was almost complete with no decrease in particle melting with a decrease in gun power. For internal injection slightly downstream of the anode arc root, nearly all particles were melted for the highest gun power tested, however the percentage of melted particles decreased with decreasing gun power. For the particles injected at the nozzle exit, significantly less particles were melted than the other two methods, and a decrease in gun power significantly decreased the amount of melted particles. For the lowest gun power that was tested, hardly any of the powder adhered to the substrate. Similarly, the coating properties for the three different injection methods were adversely effected by the two radial injection methods. The axially injected coating was mostly uniform and dense with few pores. The coating sprayed with internal radial injection was uniform but had more pores than the axially injected coating. The external radially injected coating was very porous and nonuniform. The deposition efficiencies for the three methods were 45.7% for the axially injected powder, 29.1% for the internal radially injected powder, and 11.5% for the external radially injected powder.

Numerical simulations of the three-dimensional plasma jet and particles were done by [19–21]. The three-dimensional effects of transverse particle injection cannot be ignored because the injection causes deflection of the plasma jet and particles, especially for cases of high carrier gas momentum compared to the plasma momentum. The results of Xiong *et al.* [19] will be presented here.

The setup used by Xiong *et al.* included a DC plasma spray gun with external particle injection. The two powders used for this study were NiCrAlY and $ZrO_2$. Their study

developed a three-dimensional Computational Fluid Dynamics (CFD) code that assumed no symmetry and accounted for transient in-flight particle characteristics including melting and evaporation. Their results were verified with experimental data. The results of gas temperature for the plasma jet with a constant carrier gas flow rate of 15 SLM showed that the plasma is vectored down slightly due to the particle injection. The radial displacement of the plasma jet is about 0.25 cm with 15 SLM carrier gas, and though that carrier gas flow rate is not shown in their results, the radial displacement of the particles for the nearest carrier gas flow rate (6 SLM) at the same flight distance is slightly more than that. If the trend of larger carrier gas flow rates continued through 15 SLM, the radial displacement for that flow rate would be much larger. This indicates that the particles have left the plasma jet at that flight distance.

## 2.4 Substrate Thermal Management

When molten particles are sprayed onto a solid substrate, the particles may melt the substrate and from a compound of the two materials [22–24]. This melting is beneficial to the coating adhesion strength and improves the properties of the coating. When heat from the plasma itself is transferred to the substrate, however, the substrate may experience warping and adverse melting that may ruin the part. Typically, the substrate is cooled while it is being sprayed, but this is not always sufficient to prevent damage to the substrate.

# Chapter 3

# Approach

## 3.1 Objectives

The purpose of this research is to investigate the behavior of the CSM device for small vector angles, analyze the results for repeatability of the vectored jet, and determine the effects of rotation on the vectored jet, and apply those results and the results of Allen *et al.* to design a CSM device suitable for plasma spray. The plasma spray CSM device will then be tested to determine vectoring effects on plasma spray. The objectives of the research are as follows:

- Use high speed stereo particle image velocimetry to measure the velocity field of a cross section of the vectored jet at a distance downstream of the CSM device for several Reynolds numbers and rotation rates.
- Use particle image velocimetry to measure the velocity field of the vectored jet for small angles for various geometries.
- Use the results of the particle image velocimetry to calculate the precision uncertainty in the vectored jet angle.
- Use the results of the stereo particle image velocimetry to determine the response time of the vectored jet.
- Use the results of the small angle study to design a CSM device suitable for plasma spray and test that device on a commercial plasma spray gun.
- Compare the properties of vectored and unvectored plasma spray.

The procedures to be carried out are in fulfillment of the objectives listed in this chapter. The thesis is of the further development and research of the CSM and application of CSM

technology to plasma spray. The testing will be completed through the use of a newly designed CSM test facility using the results of the previous study by [3] and a newly designed plasma spray CSM device. This chapter will outline the procedures and describe the tests that will be completed using particle image velocimetry and SprayWatch and describe the test facility. The last sections will describe the parameter space that will be investigated and analysis of the data and the method of uncertainty analysis performed on the data.

## 3.2 Design

Three major tests will be carried out: PIV, stereo PIV, and the plasma spray tests. Standard PIV will be described in detail first because stereo PIV is a more complex extension of PIV. The parameters that are varied in each test are largely geometrical, so the CSM test facility will be described as well. Finally, the methods of measuring the plasma spray results will be described.

### 3.2.1 Particle Image Velocimetry (PIV)

PIV is an optical means of measuring two-dimensional flow velocity fields. The test CSM, to be described later, is set up to direct the flow horizontally. The secondary flow is passed through a seeder that injects the flow with olive oil particles. Both the primary and secondary flows are compressed air. The device will be placed inside of an enclosure approximately 1 $m^3$ so the surrounding ambient air will be seeded as well. Two NdYag lasers are oriented vertically shining down perpendicular to the flow direction with sheet optics to create a thin laser sheet. The laser sheet illuminates a cross section of the jet in the flow direction. The laser light illuminates the olive oil particles and a snapshot of the illuminated particles is captured by a digital camera. The lasers fire two times closely together with a known time step in between. The camera and the lasers are synchronized so the camera acquires one image per laser illumination. The PIV images are then correlated to estimate the displacement between the two instances in time and the velocity field is calculated. Several of these velocity fields may be captured for each data set. The resulting velocity fields will be analyzed to determine the vector angle for each velocity field.

To analyze the velocity fields to find the vector angle, a weighted averaging scheme will be used. Each velocity vector in the velocity field will be used. For each vector, the weight will be the magnitude of the vector. This will be multiplied by the vector angle and this product will be summed for all vectors in the field. The sum of the products will be divided by the mean velocity magnitude to yield an instantaneous weighted average vector angle. For the vectors that make up the jet, the magnitude will be large compared the the vectors in the ambient surroundings. This will ensure that the average vector angle reflects the average vector angle of the jet. This averaging process will be performed for every velocity field in a given set, and then the instantaneous vector angles may be averaged throughout the set to find a total average vector angle.

### 3.2.2 Stereo Particle Image Velocimetry

Stereo PIV is a variation on PIV that can resolve the third component of velocity. PIV measures a two-dimensional velocity field with x- and y-components. Stereo PIV measures a velocity field with x-, y-, and z-components of velocity. To accomplish this, the laser plane is oriented cross stream with the flow directed through the laser sheet. Two digital cameras are required. The cameras are oriented at an angle to the laser sheet, typically around $\pm 45°$. The laser sheet is made thicker so that the displacement between images is through the laser sheet thickness. Correlation is performed between the four images (two for each camera) to find the velocity field. The Stereo PIV test is performed with the CSM rotating the vectored jet, so special timing is used so that there are 50 velocity fields per rotation, and each shot in the set of 50 correlates to the device rotated to the same position of subsequent rotations.

To determine the effects of rotation on the vectored jet, the center of velocity of each vector field will be found. Analogous to a center of mass calculation, the center of velocity calculation uses the magnitude of each velocity vector multiplied by the distance that vector is from a datum. Each product will be summed together and the sum of the products will be divided by the summation of the velocity vector magnitudes for the whole field. This will result in a location of the center of velocity. This is used as the location of the center of the jet. This process will be performed on every velocity field in the data set to essentially

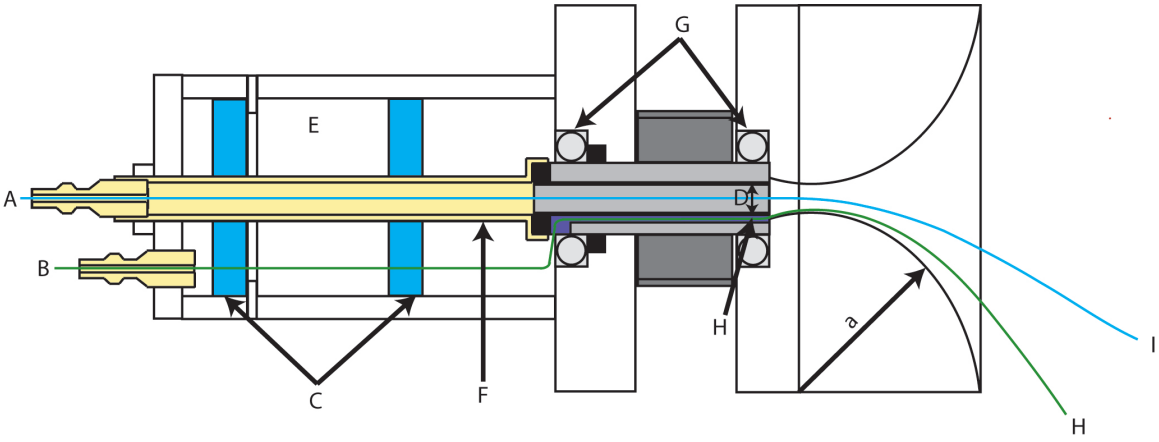


Fig. 3.1: Cross section of the CSM test facility showing the path of the primary and secondary flows.

trace the path of the vectored jet through every rotation.

### 3.2.3 Test CSM Facility

To facilitate the geometrical variations required for the parameter space that will be discussed in the Data section, a special CSM test facility was needed. In addition to accommodating various geometries, the new device also needed to be capable of rotation. A cross section of the device is shown in Fig. 3.1. The device uses compressed air for both the primary and the control flow. The primary and control flows enter the device separately shown at points A and B, respectively. The control flows through a plenum with flow conditioning diffusers shown at C to make the flow more uniform. The control flow is directed through the rotating control slot at H and exits the device near the coanda surface. The primary flows through a straight pipe to exit with diameter D. The gray middle section is fitted with a pulley and bearings at G to allow rotation. The coanda surface collar is shown with radius of curvature R. The control flow follows the curved collar as illustrated at H and the primary flow is pulled into vectored position shown at I. Except for the diffusers, bearings, seals, and pulley, the entire device is machined out of Alloy 6061 Aluminum. Several collars with various radii can be interchanged to alter the geometry as well as two different control slot sizes.

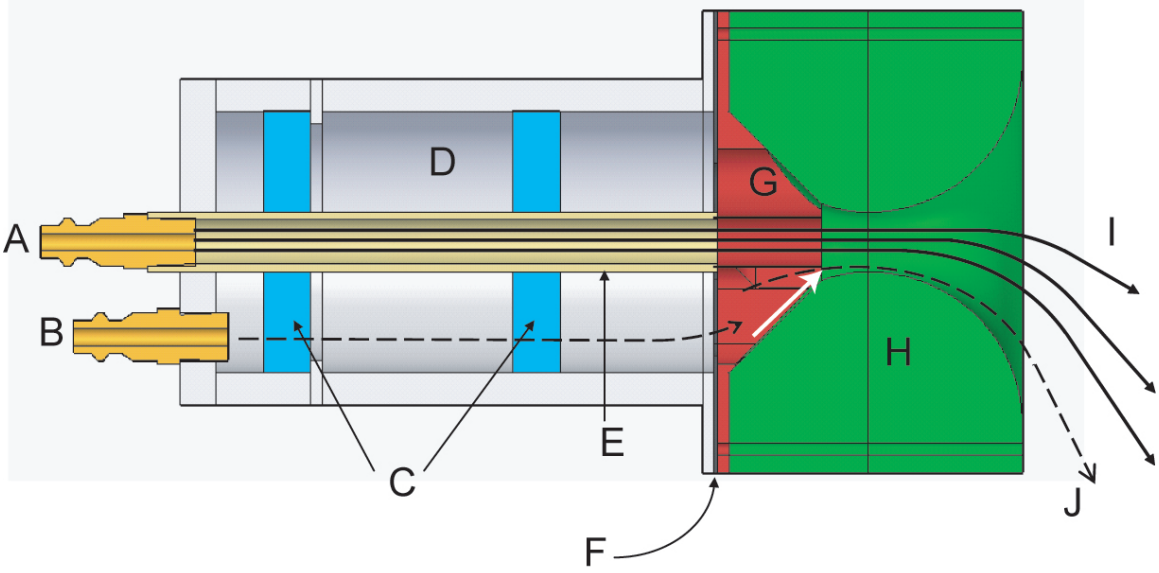


Fig. 3.2: Cross section of the CSM test facility used in the study by Allen and Smith [3] with an arrow added to show flow path problem.

The CSM test device design from the study performed by Allen and Smith [3] is shown in Fig. 3.2. In their setup, the control flow entered at B and passed through a plenum at D with flow conditioners at C. After passing through the plenum, the flow entered the control slot in part G that directed the flow to the coanda surface. In this design, however, a small problem exists. The flow over the bottom part of the control slot near the collar is in an angled direction relative to the axis of the device. When that flow reaches the control flow exit, it is still angled. The white arrow has been added to this figure to illustrate the flow direction. This causes the control flow to essentially blow across the primary flow. It has been suggested that this angled flow path may be the cause of the negative vector angles for small momentum flux ratios in the results of Allen and Smith. To correct this problem, a straight length of control slot is needed prior to the control jet exit to ensure that the flow is truly parallel to the primary flow at the exit plane. This correction has been made in the proposed design in Fig. 3.1 shown at H.

### 3.2.4 Plasma Spray Measurements

With the results of the previous two isothermal studies, a suitable CSM device was

designed for a commercial plasma spray gun. Tests to determine the effect of vectoring on the plasma spray properties and coating properties are performed.

To measure the sprayed particle temperature, velocity, and trajectory while in flight, a SprayWatch 2i [25] system was used. SprayWatch 2i is a commercial thermal spray monitoring system. A fast shutter CCD camera is used to acquire digital images of the spray. Images are taken with a short exposure time and individual particles are identified. The velocity and trajectory of these particles is determined using special proprietary algorithms. A second set of images with a longer exposure time is simultaneously taken to measure the temperature of the particles using two-color pyrometry. From the SprayWatch data, the velocity, temperature, and spray angle will be used.

To measure the deposition efficiency, a rudimentary method was used. The particle feeder feeds unheated particles into a container for a given amount of time. The container is weighed before and after particle addition to determine the mass flow rate of particles into the plasma spray gun. Coatings are formed by plasma spray for vectored and unvectored conditions with a known amount of spray time, and the mass of the substrate is measured before and after spraying. The percentage of material that adheres to the substrate may then be calculated.

After the coatings have been formed for various vectoring conditions, the coatings were sectioned, mounted, and polished. Metalographic analysis was performed on the polished sections to determine the porosity and examine the microstructure of the coatings.

### 3.3 Data

To meet the objectives of this thesis, several parameters need to be varied independently for each test. The same equipment is to be used for each test, so the CSM device has been made to accommodate various geometries as described above. The parameters that will be varied for the tests are:

- CSM geometry, specifically the control slot size and the coanda surface radius
- Momentum flux ratio

- Reynolds number of the primary jet
- Rotation rate

Allen and Smith [3] determined that the size of the control flow exit is very important to vectoring. It affected the maximum vector angle that can be achieved as well as the momentum flux ratio that was required to achieve that vector angle. Only two control slot sizes will be used in this test. From their results, the optimum control slot size will be used (30% of circumference), as well as the smallest control slot from that test (15% of circumference). The smallest control slot was selected because the vector angle results for that case showed a small change in vector angle with increasing momentum flux ratio, which is desirable in the small angle region.

Also selected from the results of Allen and Smith is the radius of curvature of the coanda surface. It has been shown that the radius of curvature of the coanda surface affects the vector angle that may be achieved. The larger the radius of curvature of the surface, the longer the flow will stay attached according to the Coanda effect. Allen and Smith selected the largest radius of curvature they tested ($5.25D$) as the optimum for vectoring. This coanda surface radius as well as the smallest radius they tested ($2.00D$) was used in this study.

The momentum flux ratio is controlled though the input flow rates for the primary and the control flows. Allen and Smith showed that this is the parameter that largely determines vector angle for each case. The momentum flux ratio was varied from 0.01 to 0.09 for the small angle study. This range was selected because the results from Allen and Smith had only two points in the range between 0 and 0.1 to produce desired angles of $0^{o}$-$10^{o}$. The vector angle results in this range were very inconsistent, in some cases vectoring in the wrong direction at this point, possibly due to the design problem discussed above. For the flame or arc realignment application to thermal sprays, this range is critical.

The Reynolds number of the primary jet was varied for the small angle study for only one geometrical configuration. This was done to observe the dependence on Reynolds number

for the small angle range. Three primary jet Reynolds numbers were used for the rotational study. The Reynolds numbers selected were 22600, 45300, and 113200.

The rotation rate for the rotation study was controlled by a stepper motor which can be programed to rotate at a specific speed. The stepper motor was fitted with a pulley to the CSM. Three different rotation rates were used in the rotation study: 300, 600, and 1200 RPM.

The data for the small angle study was acquired in four tests (two collars and two control slot sizes). Four each of the four tests, seven momentum flux ratio cases between 0.01 and 0.09 were used. For each momentum ratio case, 300 PIV image pairs were taken and analyzed to find the velocity field. From each velocity field, the vector angle was found using the weighted averaging scheme detailed above. The instantaneous vector angles were averaged to find the mean for the whole set and the precision uncertainty.

The data for the rotation study was acquired in nine tests with three rotation rates and three Reynolds numbers. For each test, the PIV images were timed so there are 20 data points per revolution of the CSM. A total of 1024 PIV image pairs will be taken and analyzed for each test. The resulting vector fields were used to find the center of velocity according to the procedure described above. The vector fields were grouped by the 50 rotational positions and the average velocity field for each position were found. Precision uncertainty information was found comparing all of the center of velocity points to find a mean radius and standard deviation for the circle traced out by the mean path of the vectored jet as it rotates.

Once the isothermal small angle data was acquired, a CSM device was designed for use on a plasma spray gun. The CSM fitted gun was used to create coatings for various control flow rates and the properties of the particles in-flight were compared as well as the coating properties for vectored and unvectored cases. Two materials were sprayed: Praxair Ni-164, which is a Ni 22Cr 10AL 1Y atomized powder with a particle size range of -106/+53 μm, and Metco 201B-NS-1, an agglomerated and sintered ZrO2 5CaO 0.5Al2O3 0.4SiO2 spherical powder with a particle size range of -90/+25 μm. All tests were performed using

the parameters recommended in the Praxair data sheets for the powder involved. No attempt was made to further optimize the spray parameters.

### 3.4 Uncertainty Analysis

The method of calculating the uncertainty of the measured variables will be described. For the PIV measurements, the bias uncertainty affects the velocity magnitude of the results. The velocity magnitude is not very important compared to the direction of the velocity for angle calculation, therefore the bias uncertainty is not used. The same argument applies to the stereo PIV measurements, where the location of the velocity is important but the actual magnitude is not. For the 2-D PIV measurements, the precision uncertainty was calculated from the mean and standard deviation of the vector angle for 300 velocity fields. For data measured by SprayWatch, the bias uncertainty was small compared to the precision uncertainty for velocity, temperature, and position. The precision uncertainty was calculated from the mean and standard deviation of 26 data points each obtained from an average of several particles. The uncertainty on primary and control flow for the PIV data was obtained from the bias uncertainty information for the Porter series 200 mass flow controller. The uncertainty on control flow for the plasma spray tests is the bias uncertainty for the flow meter used to meter the flow.

# Chapter 4

# Results

The results of this study will be presented in this section. The stereo PIV results for the rotation study will be presented, followed by the results of the small angle study. The new design for plasma spray application will be presented as well as the results from the plasma spray tests.

## 4.1 Rotation and Response Time Study

Three rotation rates and three Reynolds numbers were tested and the results are shown in Fig. 4.1 grouped by rotation rate. The mean radius of the circle traced out by the center of velocity locations was calculated and the results are shown in Table 4.1. The RMS of the 20 data points at each circumferential location was calculated and the results are nondimensionalized by the mean radius are shown in Fig. 4.2. The data from Fig. 4.1 are replotted grouped by Reynolds number shown in Fig. 4.3.

When grouped by Reynolds number, it is apparent that rotation rate has little effect on the mean radius of the centers of velocity. For the highest Reynolds number case, the mean radius is much larger than for the smaller two Reynolds numbers, indicating that the vector angle for the highest Reynolds number is larger than for the other two cases. The vector angle appears to be inconsistent with rotation angle for the highest Reynolds number case (as can be seen by the center of velocity locations tracing a pattern that is not quite circular), especially for 300 and 600 RPM. For the two smaller Reynolds numbers, the vector angle appears to be consistent for each circumferential position for the three rotation rates. The RMS plots indicate circumferential positions that have vectoring inconsistency. For the 22600 and 45300 Reynolds number cases, these positions appear to be fairly random and do not correlate to the circumferential locations of the vectoring inconsistencies for the 113200

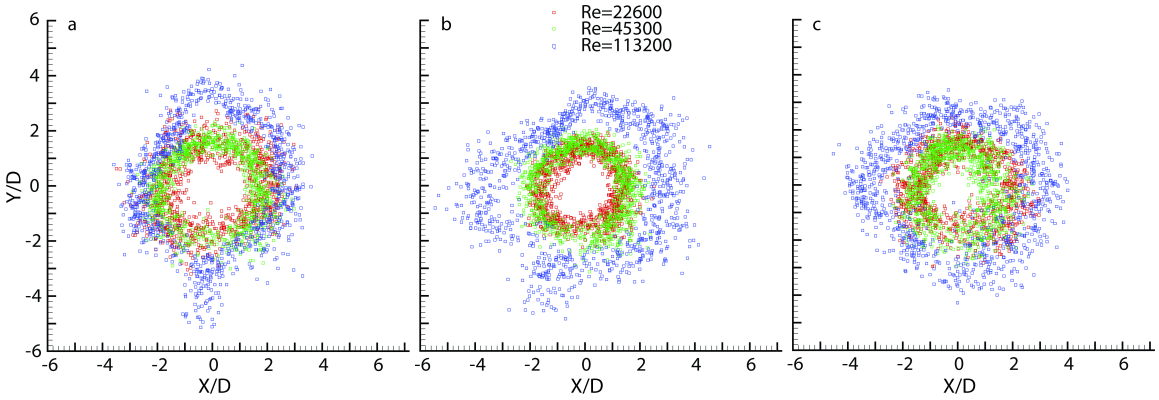


Fig. 4.1: Center of velocity data grouped by rotation rate for a) 300 RPM, b) 600 RPM, and c) 1200 RPM.

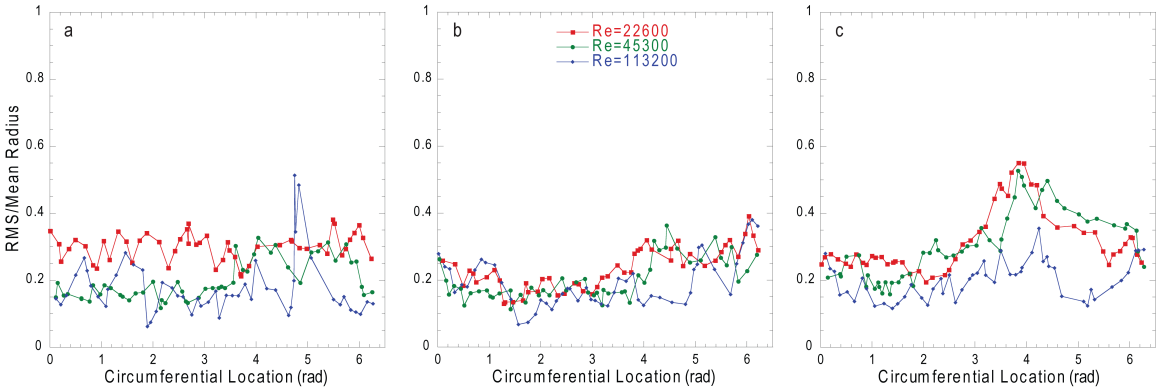


Fig. 4.2: RMS of center of velocity data grouped by rotation rate for a) 300 RPM, b) 600 RPM, c) 1200 RPM.

Reynolds number case. These changes in vector angle with circumferential position could be due to geometrical inconsistencies.

n

To determine the effect of rotation rate, a time scale for the device is defined as

$$\tau = \frac{L}{u} \tag{4.1}$$

where $L$ is a characteristic length and $u$ is the mean velocity of the primary flow. The length of the collar was selected as a suitable characteristic length. For collars extended to 90° that

Table 4.1: Mean radius results for center of velocity data.

| 300 RPM | | 600 RPM | | 1200 RPM | |
|---|---|---|---|---|---|
| Re | Mean Radius | Re | Mean Radius | Re | Mean Radius |
| 22600 | 1.7538D | 22600 | 1.3845D | 22600 | 1.5621D |
| 45300 | 1.8417D | 45300 | 1.6848D | 45300 | 1.4637D |
| 113200 | 2.8085D | 113200 | 3.1688D | 113200 | 2.7632D |

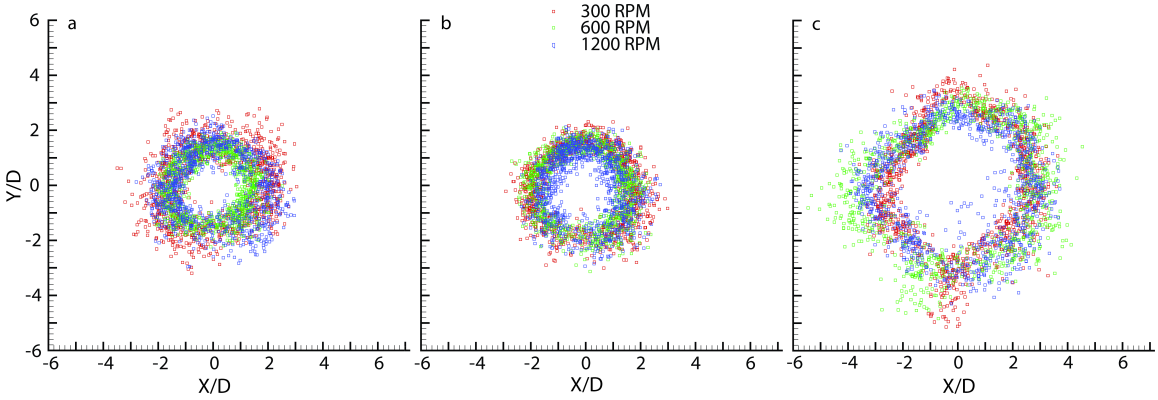


Fig. 4.3: Center of velocity data grouped by Reynolds number for a) 22600, b) 45300, and c) 113200.

were used in the isothermal studies, $a$ is the length of the collar, making

$$\tau = \frac{a}{u}. \tag{4.2}$$

Assuming that the flow velocity remains roughly constant, the time it takes the flow to move from the exit of the jet to the end of the collar is $\tau$. $\tau$ may be compared to the time per revolution $t$

$$\frac{t}{\tau} = \frac{1}{\omega\tau} \tag{4.3}$$

where $\omega$ is the rotation rate. For the fastest rotation case (1200 RPM) and a Reynolds number of 113200, the number of time constants per revolution is approximately 19. Looking at it another way, for a control slot that is 30% of the circumference, a given point on the circumference has control flow for about $5.8\tau$. This is sufficient for the flow to be fully vectored. The lower the primary velocity, the fewer time constants are in a given rotation. For a Reynolds number of 22600, there are only $4\tau$ per revolution, and a given point on the

circumference has control flow for about 1.2τ. In general, it can be seen that the response time of the vectored jet scales with the reciprocal of the velocity of the primary jet. For a lower velocity primary jet, 1200 RPM might be too fast for the jet to respond. However, most thermal spray processes of interest have very large velocities.

### 4.2 Small Angle Study

Two collar radii and two control slot sizes were used for the small angle study. The vector angles were calculated as described above. The averaged results are shown in Fig. 4.4 for a Reynolds number of 45300. The vector angle is a strong function of momentum flux ratio for all cases with a roughly linear trend. The data in Fig. 4.4 for $a/D = 2.0$ and 30% circumference show a region of negative vector angle and a large increase in vector angle with a small increase in momentum ratio in the region of $J^* = 0.07 - 0.08$. This is undesirable because vector angle in this range becomes difficult to predict. For $a/D = 5.25$ and 15% circumference, there is a large discontinuity in the range of $J^* = 0.03 - 0.04$, which causes difficulty predicting the vector angle in that range. For the $a/D = 5.25$ and 30% circumference and $a/D = 2.0$ and 15% circumference cases, the trend is fairly smooth with no discontinuities and a small slope. The geometric parameters selected for the plasma spray CSM device were collar radius ratio of $a/D = 2.0$ and a slot circumference of 15% because it performed as desired: a range of momentum ratios over which control is proportional and stable. The trend for this case has a small slope, meaning that small variations in the momentum flux ratio have little effect on the vector angle compared to cases with higher slopes, leading to more stable vectoring.

Additional data sets were acquired for the $a/D = 2.0$ and 30% circumference case. Two data sets were taken with the same parameters to check the reproducibility at a Reynolds number of 45300 and then two additional sets were taken, one with a higher Reynolds number of 67900 and one with a lower Reynolds number of 22600. The averaged results are shown in Fig. 4.5. The results agree within the uncertainty bars for about half of the data points for the repeated case, indicating that the precision uncertainty bars with 95% confidence do not include 95% of the data. This would indicate that there is an uncertainty

associated with repeatability that is not being accounted for with the current analysis. This repeatability uncertainty indicates that the measurement is sensitive to parameters that are not quantified. Because the precision uncertainty bars to not include the mean for the two sets, it can be deduced that short term statistics are not indicative of repeatability. The shapes of the data trend for the repeated cases are similar enough that correct observations about the behavior may be made.

For the lower Reynolds number case, the data match well with the repeated baseline cases about as well the baseline cases match each other. For the 67900 Reynolds number case, the data does not match the other results well at all. The shape of the trend is similar, but the results appear to be offset from the other Reynolds number cases. This would indicate that the results do not extend over various Reynolds numbers, which is in agreement with the results from the rotation study given above. For the large angle study performed by Allen and Smith [3], Reynolds number was not investigated as a parameter affecting vector angle. This approach made more sense for the large angles study because their aim focused on determining the largest possible vector angle and the effects of vectoring. For small angles or applications where it is desired to finely tune vector angle, this information is important. For higher Reynolds numbers, it could be expected that the jet would stay attached to the curved surface longer because of the very thin boundary layer. It is probable that there is limit beyond which vectoring achieves Reynolds number independence, but this value is not currently known.

The vector angles plotted in Figs. 4.4 and 4.5 are averaged over 300 velocity fields for each case. Each individual velocity field was analyzed to find the instantaneous average vector angle for that field. The instantaneous averages were averaged over time to find the averages shown in those figures. The instantaneous averages were distributed about the mean. Sample distributions for one geometrical configuration and two momentum flux ratios are shown in Fig. 4.6. The skewness and kurtosis of each distribution was measured and is tabulated in the appendix along with the vector angle and standard deviation. The distributions were generally Gaussian and the skewness and kurtosis did not vary much

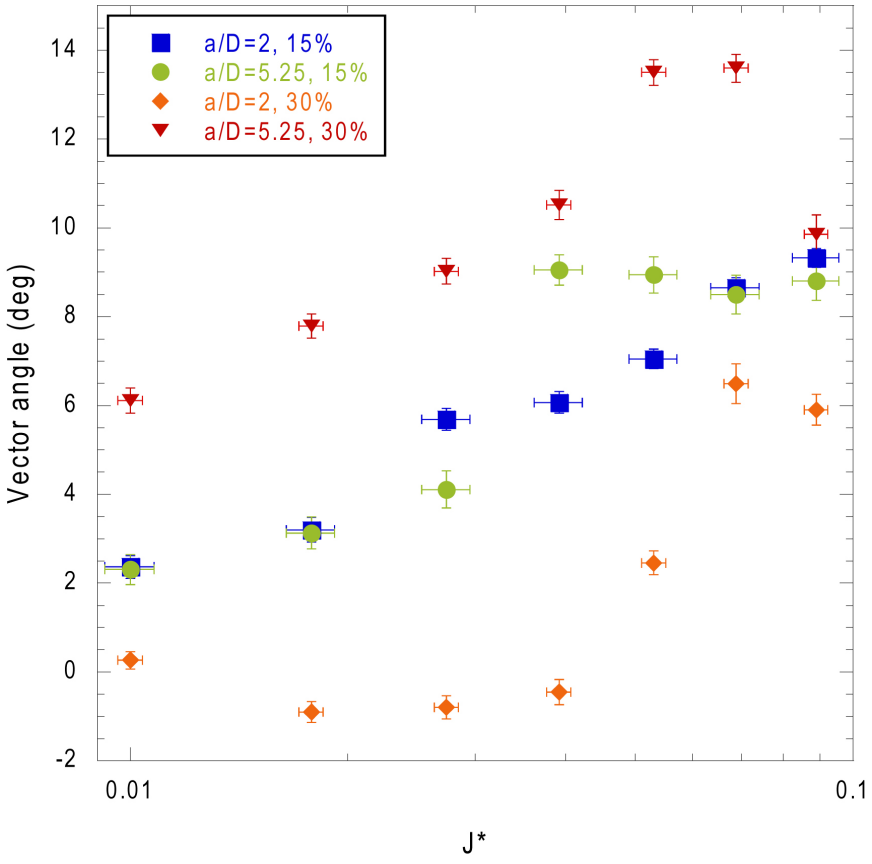


Fig. 4.4: Vector angle as a function of momentum ratio for two collar radii and two control slot sizes.

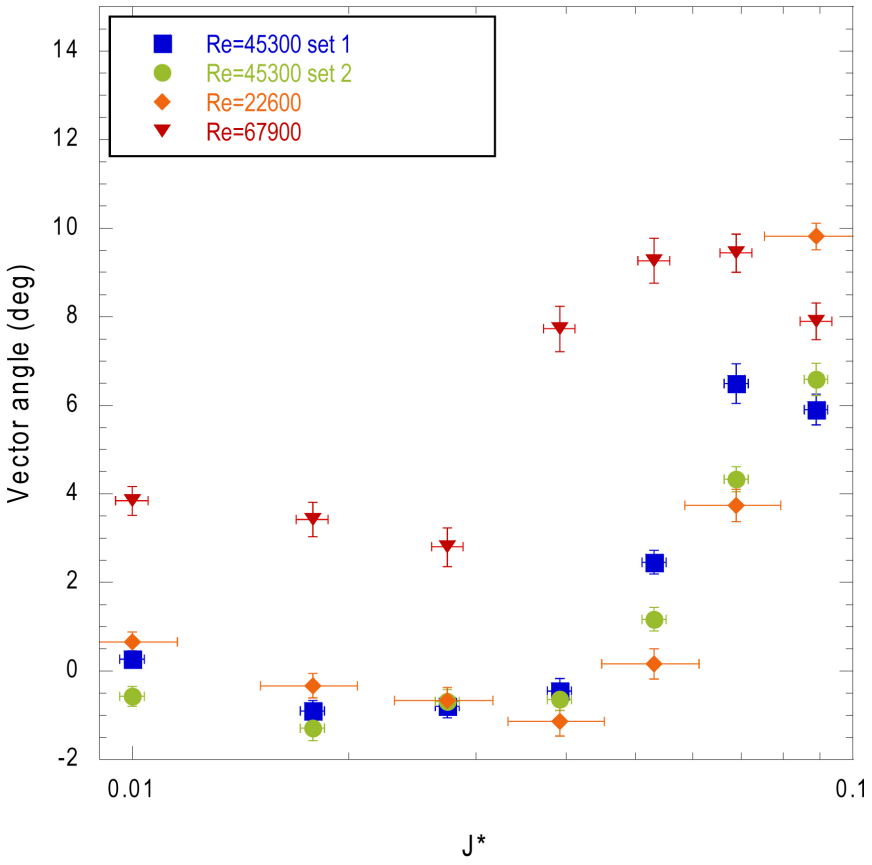


Fig. 4.5: Vector angles as a function of momentum ratio for $a/D = 2.0$ and 30% circumference for three Reynolds numbers.

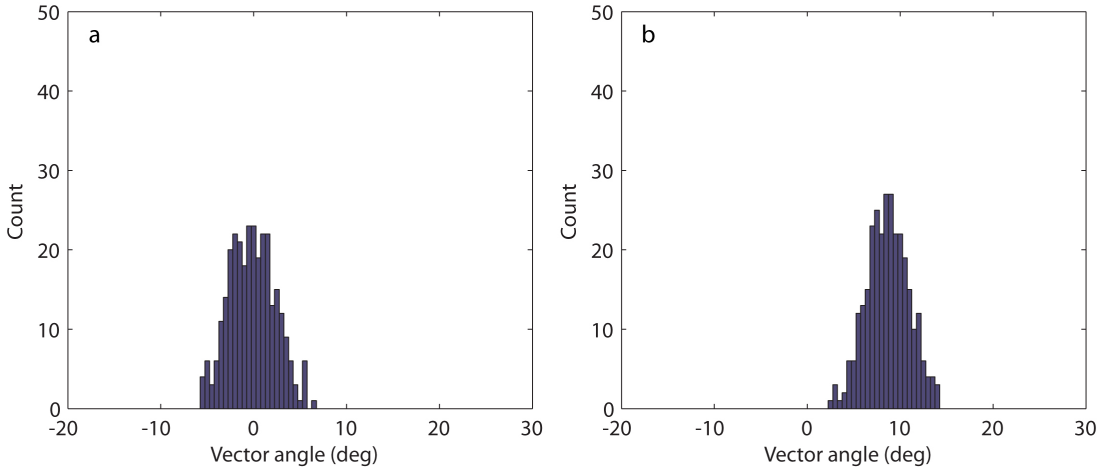


Fig. 4.6: Distribution of instantaneous vector angle for a) $J^* = 0.01$ and b) $J^* = 0.09$ for $a/D = 2.0$ and 15% circumference.

across momentum flux ratio. The standard deviation increased with momentum flux ratio for every case except the $a/D = 2.0$ and 15% circumference case. For this reason this geometric configuration was selected for the plasma device design.

### 4.3 Design of Plasma Spray CSM Device

From the results of the small angle study and from the results of Allen and Smith [3], two devices suitable for use on a commercial plasma spray gun were made. The plasma spray gun used for this study is the Praxair SG-100 DC plasma spray gun. The gun comes with a standard copper face plate that is replaced by the newly designed device. The SG-100 uses cooling water to cool its internal components, but additional cooling water is needed for the new devices to prevent melting.

Two devices were designed for use with a plasma spray gun. The first device was intended for large angle vectoring to achieve vectoring of plasma and particles to large angles. This could be used to change the spray angle or possibly address substrate and particle thermal management. The second device used the results of the small angle study to design a device intended for vectoring between 5-10°. This device is intended to realign the plasma with the particle trajectory.

From the results in the small angle study, design parameters were chosen to be $a/D = 2.0$ and 15% control slot circumference for the small angle device. For the large device, the optimum for maximum vectoring as determined by Allen and Smith [3] ($a/D = 5.25$ and 30%) will be used. The CSM device design uses two parts for both small and large angle designs, both machined out of oxygen-free 101 copper. The bottom part attaches to the plasma spray gun sealing off the cooling channels and routes the control flow in from the radial direction. The top part mainly consists of the coanda surface. Both parts use standard o-rings to seal all surfaces.

Sketches of the critical parameters and photos of the devices attached to the SG-100 plasma spray gun are shown below in Fig. 4.7. The streamwise extent of the collar should be minimized to reduce weight and bulkiness, but also to reduce added standoff distance. To minimize the length of the collar, the curved Coanda surfaces are not extended to the full 90°. For the small angle device, the collar is only extended to the thickness that is needed to accommodate cooling water channels. For the large angle device, 45° was selected as the desired vector angle for this study, so the collar need not be extended further.

The shape and dimensions of the jet exits are shown in Fig. 4.8 for both devices. The gap between the jets is ideally very small to enhance entrainment between the two jets, however this component is very near the high temperature plasma and therefore is susceptible to melting. This component was made to the minimum thickness that could be expected to withstand the high temperatures, which was chosen to be 0.056".

To ensure the control flow was tangential to the Coanda surface, the control slot must have a straight vertical length before exiting. This length was small in keeping with the object to minimize the streamwise length of the device. To accomplish this, a "boss" was designed. This boss extended into the control slot from the top part and has the effect of turning the control flow downward before routing it back upward as shown in Fig. 4.9. As a result, the control flow has a relatively long run of vertical flow prior to exiting along the collar, ensuring that the control flow direction is tangential at the exit. The boss is implemented for both devices similarly.

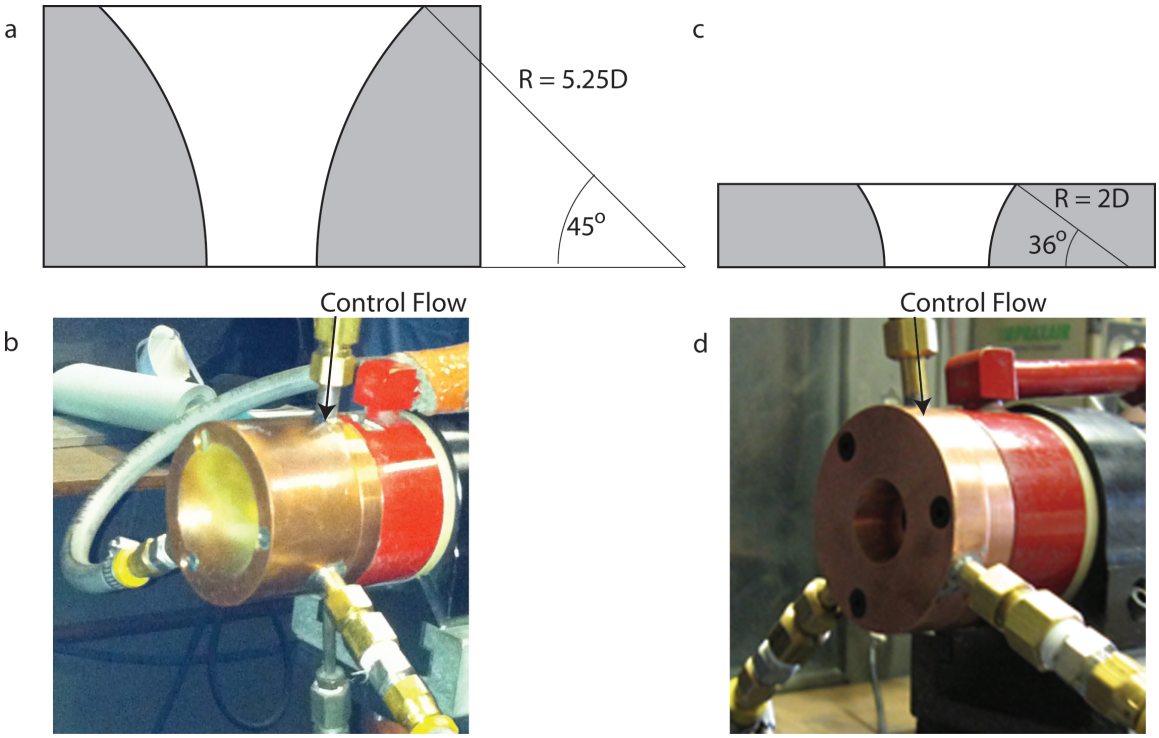


Fig. 4.7: Illustrations showing the radius of curvature and extent of the two plasma spray devices as well as photos of the devices mounted to the Praxair SG-100 plasma spray gun for a-b) the large angle device, c-d) the small angle device.

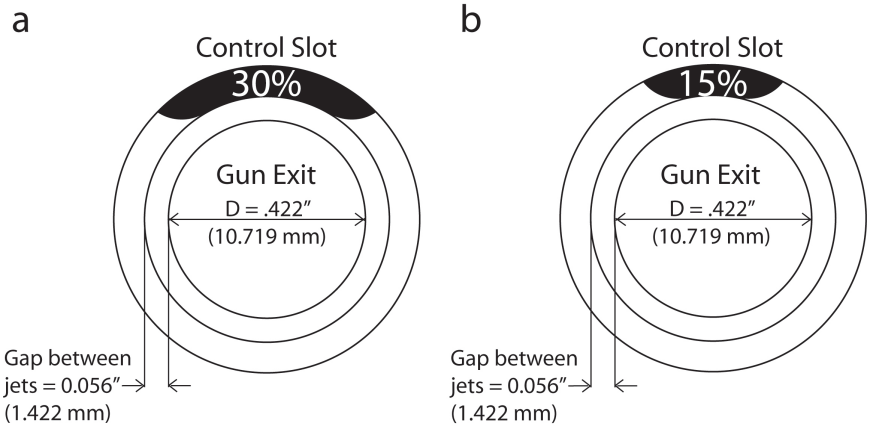


Fig. 4.8: Illustration showing the control slot size and plasma jet exit dimensions for the a) large device and b) small device.

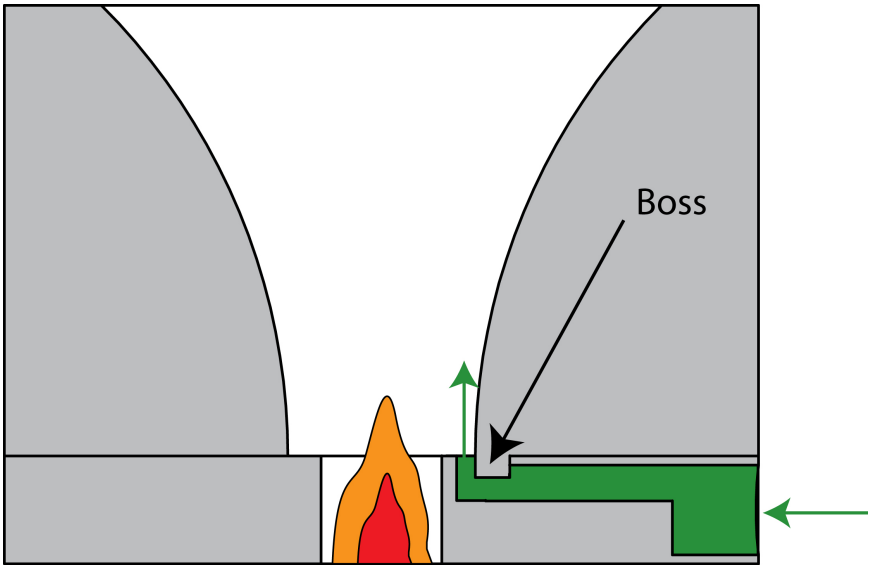


Fig. 4.9: Cross sectional view of the large angle device to illustrate the boss design and the control flow entering from the radial direction and exiting tangential to the Coanda surface.

In addition to the necessary flow design aspects, cooling water channels were added to both parts to prevent damage to the CSM during operation. The cooling water from the plasma spray gun cooled the back of the bottom part. This cooling water channel was extended further into the bottom part to aid heat transfer from the small wall separating the primary and control flow. A U-shaped groove was machined into the back of the bottom part with the middle of the U oriented away from the control slot. To cool the top part, an additional cooling water source and sink is needed. The cooling channel is machined into the bottom of the top part in a U-shape, with the middle of the U oriented towards the control slot to cool the hottest part of the Coanda surface when the plasma is vectored. Photos of the machined parts are available in the Appendix.

### 4.4 Plasma Spray Study

The plasma spray device described in the previous section was implemented on the Praxair SG-100 plasma spray gun and tested in the facilities of Plasma Processes inc, Huntsville AL. A table describing the parameters used for all permutations is shown in Table 4.2. No powder was used for the supersonic tests.

Table 4.2: Plasma spray and CSM parameters for all tests.

| Case | Collar Radius/ Slot Size | Material | Subsonic or Super-sonic | Primary Gas Flow Rate ($m^3/hr$) | Auxiliary Gas Flow Rate ($m^3/hr$) | Carrier Gas Flow Rate ($m^3/hr$) | Volts/ Amps |
|---|---|---|---|---|---|---|---|
| 1 | 2.0D/15% | Zirconia | Subsonic | 1.982 | 0.736 | 0.368 | 44/900 |
| 2 | 2.0D/15% | NiCrAlY | Subsonic | 2.832 | 1.444 | 0.297-0.340 | 40/800 |
| 3 | 5.25D/30% | NiCrAlY | Subsonic | 2.832 | 1.444 | 0.297-0.340 | 40/800 |
| 4 | 2.0D/15% | N/A | Supersonic | 5.805 | 1.557 | 0.765 | 62/900 |
| 5 | 5.25D/30% | N/A | Supersonic | 5.805 | 1.557 | 0.765 | 62/900 |

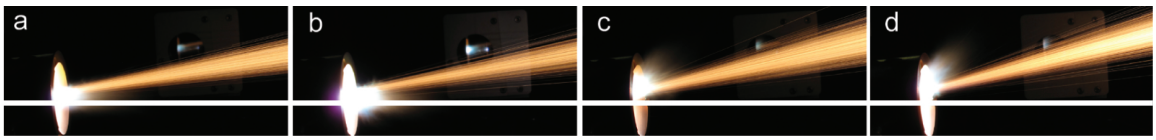


Fig. 4.10: Photo images of the case 3 (NiCrAlY, 5.25/30%) test showing the response of the plume and powder to increasing control flow rates. Flow rates for the control gas for the images are: a) 0 CFH (0 $m^3/hr$), b) 75 CFH (2.124 $m^3/hr$), c) 100 CFH (2.832 $m^3/hr$), d) 150 CFH (4.248 $m^3/hr$).

Figure 4.10 and Fig. 4.11 show the plasma spray with increasing control flow for case 3 (NiCrAlY, 5.25/30%) and case 1 (Zirconia, 2.0/15%), respectively, from Table 4.2. A horizontal line has been added as a reference to better observe the vector angle to both figures. For no control flow, shown in part a of Fig. 4.10, the powder is vectored substantially due to cross-stream injection of the powder. With the large collar, the plasma plume is eventually vectored to $45^o$ (the limit of the collar, part d), while the powder is vectored to a smaller angle. Because the drag of the particles in the plasma is low, the particles do not follow the vectored flow, although their direction is modified substantially as shown below. For case 1 (Zirconia, 2.0/15%) in Fig. 4.11 the observed vector angles for both the plasma and the particles are very small. The particles appear to be aligned well for the highest vectored case (part d).

The SprayWatch system previously described was used to measure the velocity, temperature, and angle of the particles exiting the gun. Data from case 3 (NiCrAlY, 5.25/30%) are shown in Fig. 4.12 with 95% confidence precision uncertainty bands in the vertical direction. These data show the strong relationship between the particle angle and the control flow.

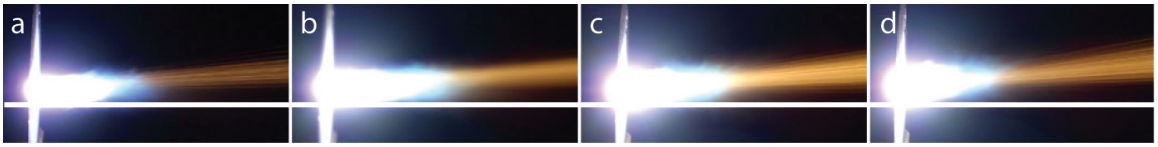


Fig. 4.11: Photo images of the case 1 (Zirconia, 2.0/15%) test showing the response of the plume and powder to increasing control flow rates. Flow rates for the control gas for the images are a) 0 CFH (0 $m^3/hr$), b) 30 CFH (0.850 $m^3/hr$), c) 60 CFH (1.699 $m^3/hr$), d) 90 CFH (2.549 $m^3/hr$).

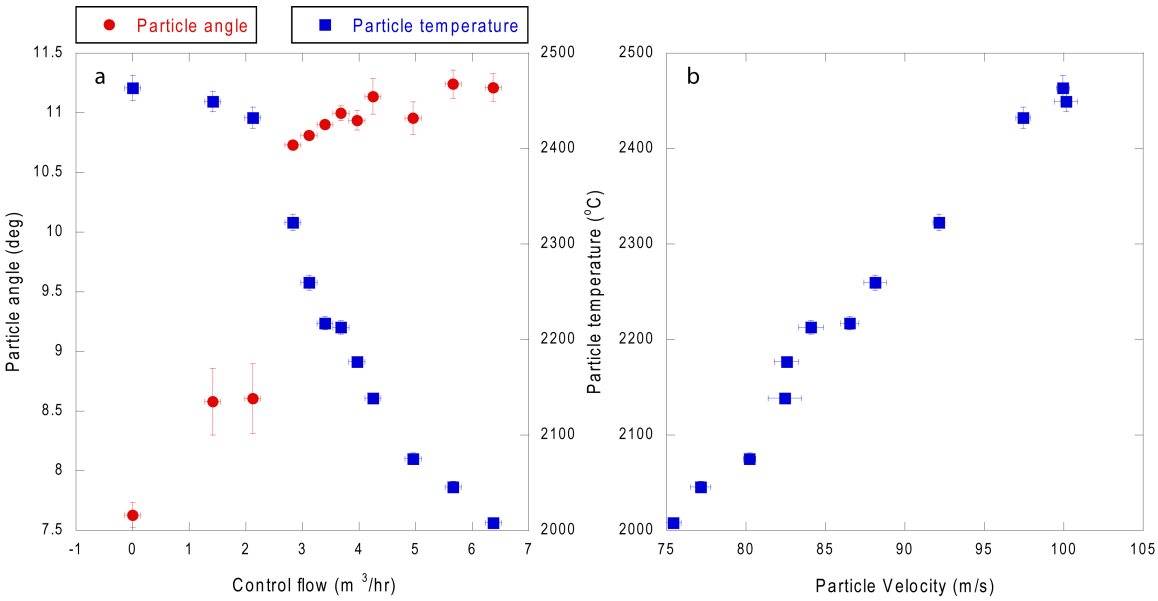


Fig. 4.12: Angle, velocity, and temperature resits for case 3 (NiCrAlY, 5.25/30%).

Note that, due to the cross-stream injection used in the SG-100, the powder is vectored to 7.5° in the absence of control flow. Adding control flow causes the powder vector angle to increase. Based on the photographs shown in Fig. 4.10, the plasma vector angle increases to a much larger angle (approximately 45°, which is the full extent of the collar). Part a of Fig. 4.12 also shows that as the vector angle of the powder is increased, the particle temperature decreases. Based on the photographs of this case, we interpret this to be due to the powder leaving the plasma plume more quickly than for the unvectored case. Simultaneously, the velocity of the particles is also decreased. Part b shows the direct relationship between the particle temperature and velocity, which is strongly linear.

Similar data were acquired for case 1 (Zirconia, 2.0/15%), and the effect of the control

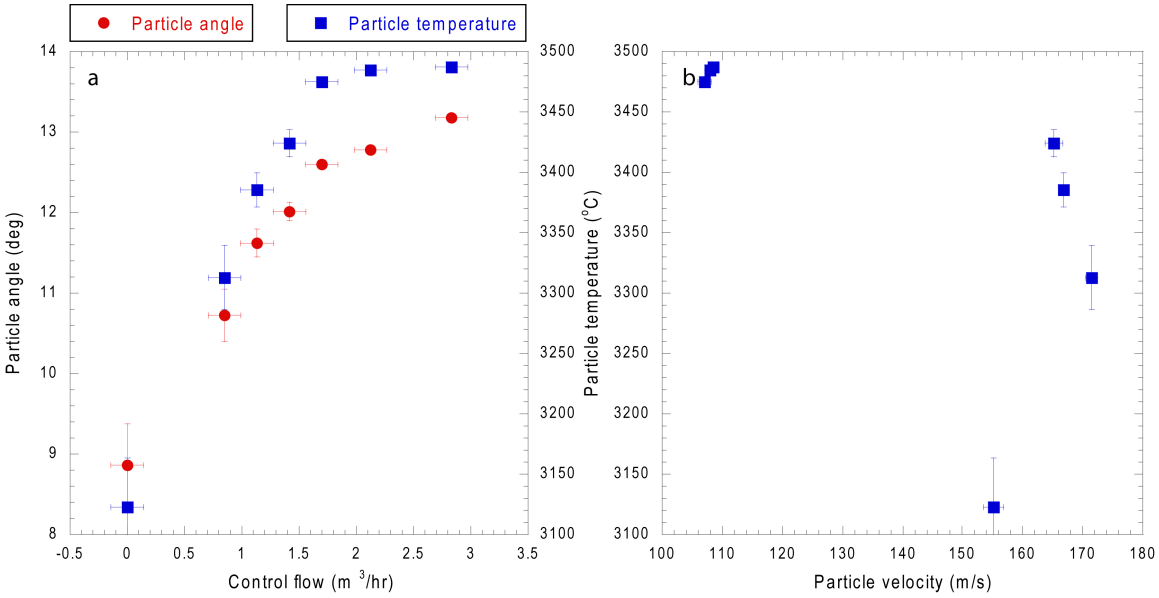


Fig. 4.13: Angle, velocity, and temperature results for case 1 (Zirconia, 2.0/15%).

flow on the particle temperature and angle are shown in Fig. 4.13. Note that this case uses the small collar and a different (less dense) material. The powder vector angle without control flow is larger (about 10.7°). Note that the intent of the small collar was to provide the ability to "realign" cross-injected powder with the plasma plume, and based on these data, it appears this has been achieved. Specifically, increasing the powder angle also increases its temperature. This is counter to the results for the large collar shown above, which is to be expected since the vector angles were much larger in that case. Part b shows the relationship between velocity and temperature. For small angle vectoring, it appears that the velocity and temperature are not correlated as they were for large angle vectoring. This may be due to the small control flow values needed for small angle vectoring.

It was postulated that an increase in the particle energy (kinetic and thermal) could result in improved deposition efficiency. The deposition efficiency was determined according to the procedure outlined above, and is shown in Fig. 4.14 for case 1 (Zirconia, 2.0/15%) and case 2 (NiCrAlY, 2/15%). For both cases with increasing control flow, it appears that the deposition efficiency is neither significantly increased nor decreased by the addition of control flow. Similar results were found for the surface roughness of the deposited material.

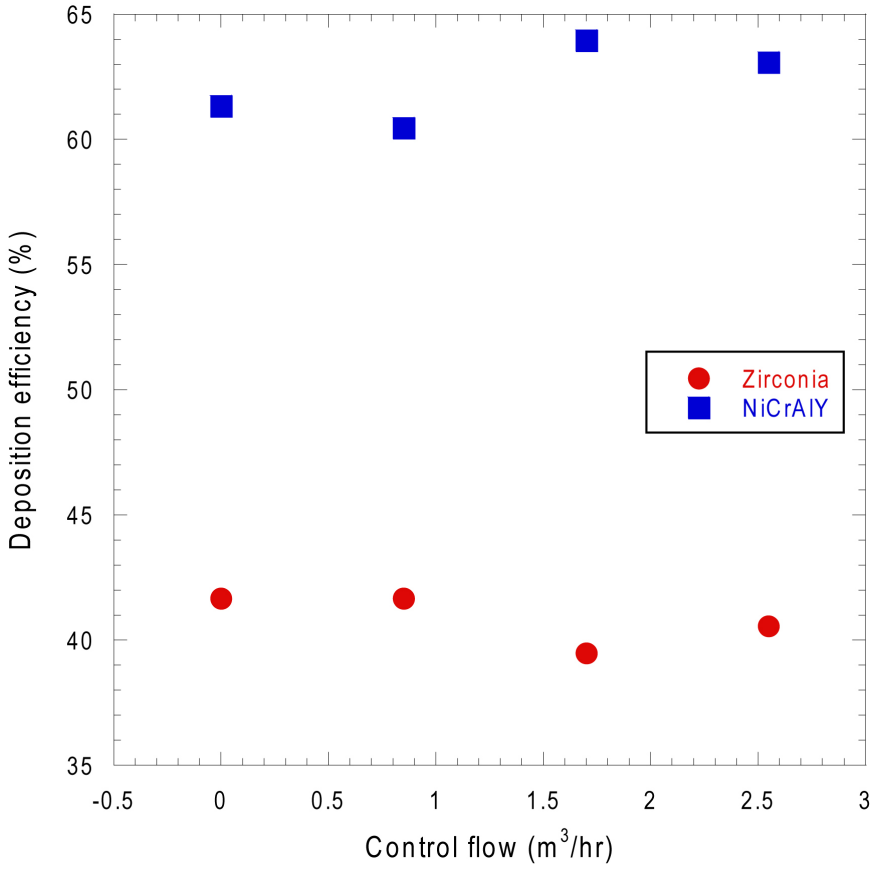


Fig. 4.14: Deposition efficiency with increasing control flow for case 1 (Zirconia, 2.0/15%) and case 2 (NiCrAlY, 2.0/15%).

This shows that the temperature and velocity changes that occurred with the inclusion of control flow in Figs. 4.12 and 4.13 do not affect the deposition efficiency or surface roughness of the deposited coating. So while the powder is better aligned with the plasma, no effect from this realignment (positive or negative) was found.

The microstructures of zirconia coatings are very dependent on the morphology and particle size distribution of the starting powder and the plasma gun parameters. Coating samples prepared according to case 1 (Zirconia, 2.0/15%) were sectioned, mounted and polished for metallographic analysis as described by Mabey *et al* [26]. The zirconia coatings exhibited typical amounts of porosity for thermal barrier coatings deposited from agglomerated and sintered powders. Compared to the baseline coating, a greater amount of porosity is observed in the zirconia coating deposited with vectoring. This is also indicated by the

lower coating density, as measured by image analysis, for the zirconia coating deposited with vectoring.

Coating samples prepared according to case 2 (NiCrAlY, 2.0/15%) were sectioned, mounted and polished for metallographic analysis as described by Mabey *et al.* [26]. The microstructures of these NiCrAlY coatings exhibit typical amounts of porosity, oxides, and inclusions for metallic coatings deposited by air plasma spray processes. Some unmelted or partially melted powder particles are also observed. The substrates for the coatings deposited with vectoring were angled $6^{o}$ relative to the plasma gun so that the impingement angle of the vectored particles remained normal with respect to the substrate surface. The microstructures of the samples deposited with vectoring are consistent with the baseline microstructure. In one coating run, the plasma gun power was increased to compensate for the temperature decrease that was measured during vectoring. This was done to produce a coating in which the temperature of the vectored particles was the same as the temperature of the baseline particles at impact with the substrate. The coating microstructure of this sample was also consistent with the baseline microstructure. The relative coating density, measured by image analysis, for these samples shows no difference between the baseline and vectored samples.

Lastly, both CSM collars were tested with the supersonic plasma configurations as described in Table 1. The fluid mechanics of supersonic flow are fundamentally different than subsonic flow. The purpose of these tests was simply to determine if CSM works in supersonic flow, and therefore no powder was added to the flow. Photographs of the unvectored and vectored flow were acquired and are shown in Fig. 4.15 and Fig. 4.16 with a horizontal reference line for case 4 (supersonic, 2.0/15%) and case 5 (supersonic, 5.25/30%) respectively. Both figures show the vectored plasma plume with an increase in vector angle compared to the unvectored case. The performance of the small collar tested as case 4 (supersonic, 2.0/15%) was essentially the same as for subsonic flow; it was possible to proportionally vector the flow but the visible vector angle was very small. For the large collar case 5 (supersonic, 5.25/30%), the flow was more prone to attach to the collar than

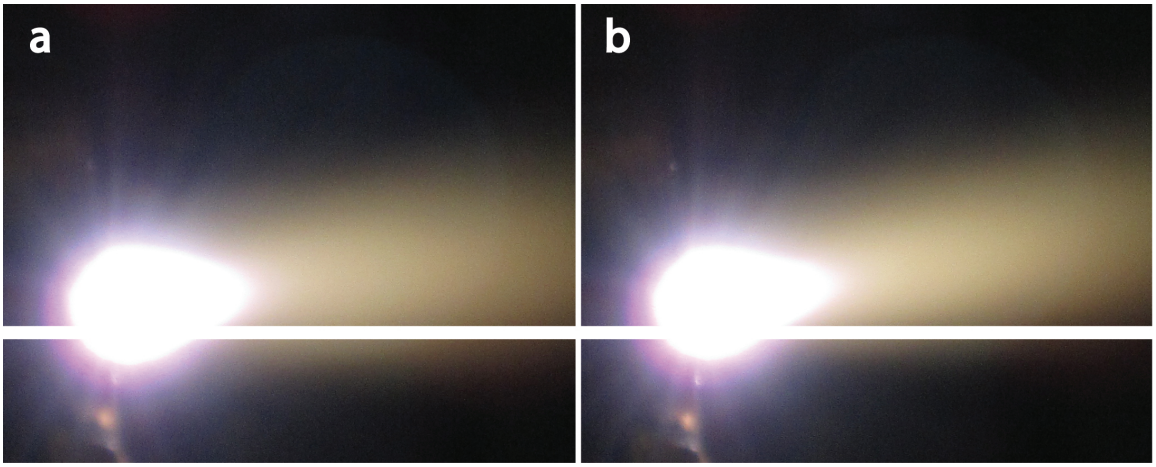


Fig. 4.15: Photo images of the case 4 (supersonic, 2.0/15%) tests showing a) the unvectored plasma and b) the plasma vectored up slightly.

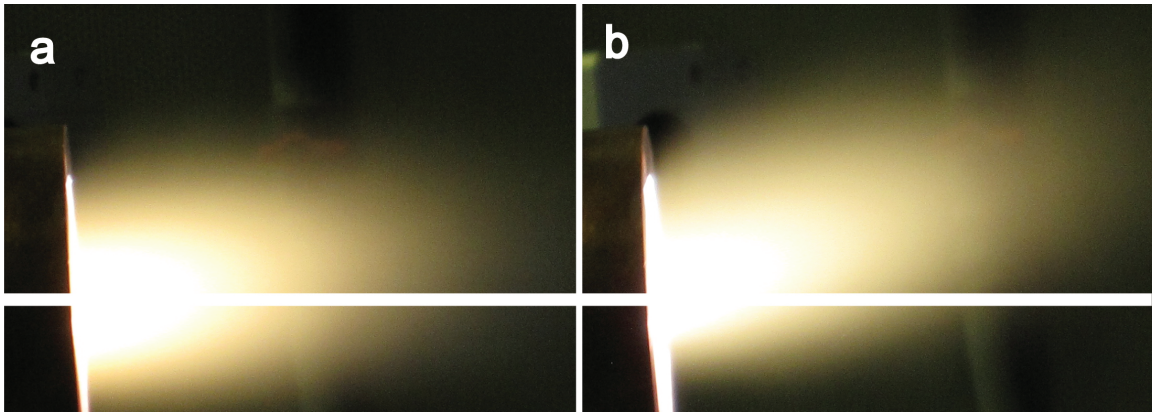


Fig. 4.16: Photo images of the case 5 (supersonic, 5.25/30%) test showing a) the unvectored plasma and b) the plasma vectored to approximately 45°.

in the subsonic cases. As a result, the flow could be vectored to 45º, but not to angles less than 45º. It is likely that the supersonic flow at the exit of the gun entrains ambient air more readily, leading to full attachment. This could be countered by having a larger gap between the plasma and the control slot or using a smaller collar radius.

# Chapter 5

# Conclusions and Future Work

A flow control method called Coanda-Assisted Spray Manipulation is further investigated. Isothermal compressed air tests were performed for four geometric permutations and seven momentum flux ratios to determine the behavior of vectoring a jet to small angles. Additional data points for the case of $a/D = 2.0$ and 30% were taken for the three Reynolds numbers. This indicated that precision uncertainty may not be used to predict the repeatability of the vector angle. The repeatability uncertainty is larger than the precision uncertainty for the case tested. Rotational tests were performed for three different Reynolds numbers and three different rotation rates. The rotation rate appears to have no effect on the vector angle or variation of the vector angle. It did become apparent from the rotation test that Reynolds number plays a large role in the vector angle that can be expected for the same momentum ratio.

The optimum parameters for small angle vectoring were determined to be $a/D = 2.0$ and 15% control slot size. This case yielded vectoring results that were linear with a small slope with little change in the spread of the instantaneous vector angle data with increasing vector angle. These parameters were used to design a CSM device suitable for plasma spray application to vector to small angles. The results from the study by Allen and Smith [3] were used to design a CSM device to vector plasma spray to large angles, up to 45°. The devices were manufactured and retrofitted to a commercially available plasma spray gun. This retrofit requires new O-rings, new mounting screws, a cooling water source and sink, and a metered control flow. The CSM devices were able to manipulate the trajectory of the plasma in the same way that was found with isothermal compressed air and the designed CSM device was able to withstand the harsh plasma temperatures and environment. The two CSM devices were used to determine the effect of vectoring on the plasma, particles,

and coating produced.

The plasma spray test results showed less dense powders vector more than denser powders, as expected. The CSM collar can be designed and operated under conditions in which the control flow can be used to manipulate the temperature and velocity of the powder particles, in addition to the spray or vector angle.

The control flow can be used to vector the direction of the particles, thus maintaining a normal impingement angle during coating deposition without moving the plasma gun. This vectoring does not significantly cool or spread the particle stream and has essentially zero impact (negative or positive) on the coating properties. The magnitude of the vectoring can be influenced by the powder particle size and density in addition to the amount of control flow and the physical design of the CSM collar.

The control flow can be used to vector the plasma jet to large angles. Under appropriate conditions, the plasma plume can be vectored to the full extent of the collar; however the particles will vector less due to their low drag in the plasma. This allows for coatings to be deposited with less direct heat transfer from the plasma to the substrate.

CSM technology offers new process control parameters for the thermal spray industry. Specific CSM parameters can be customized for the plasma spray application and the desired manipulation. Particle temperature, velocity, substrate temperature, and impingement angle could be finely tuned with CSM technology. This technology has been shown to address substrate thermal management and particle impingement angle, however it did not appear to effect the coating properties when the powder and plasma jet were realigned, neither positively nor negatively.

Future work to further understand the behavior of the CSM is needed in determining the relationship between Reynolds number and vector angle. The parameter $J^*$ does not appear to collapse all the results to a single trend. Also, the ability to manage the temperature of the substrate was not investigated, therefore further research in that area is needed.

## Bibliography

[1] Fauchais, P., "Understanding Thermal Spraying," *Journal of Applied Physics D: Applied Physics*, Vol. 37, 2004, pp. 86–108.

[2] Leigh, S. and Berndt, C. C., "Evaluation of Off-Angle Thermal Spray," *Surface and Coatings Technology*, Vol. 89, 1997, pp. 213–224.

[3] Allen, D. and Smith, B. L., "Axisymmetric Coanda-Assisted Vectoring," *Experimental Fluids*, Vol. 46, No. 1, 2009, pp. 55–64.

[4] Newman, B. G., "The Deflexion of Plane Jets by Adjacent Boundaries - Coanda Effect," *Boundary Layer and Flow Control*, Vol. 1, 1961, pp. 232–264.

[5] Juvet, P. J., *Control of High Reynolds Number Round Jets*, Ph.D. thesis, Stanford University, 1994.

[6] Kang, C. W. and Ng, H. W., "Splat Morphology and Spreading Behavior due to Oblique Impact of Droplets onto Substrates in Plasma Spray Coating Process," *Surface and Coatings Technology*, Vol. 200, 2006, pp. 5462–5477.

[7] Bussmann, M., Chandra, S., and Mostaghimi, J., "Numerical Results of Off-Angle Thermal Spray Particle Impact," *International Thermal Spray Conference Proceedings*, 1999, pp. 783–786.

[8] Hasui, A., Kitahara, S., and Fukushima, T., "On Relation Between Properties of Coatings and Spraying Angle in Plasma Jet Spraying," *Transactions of Natural Research Institute for Metals*, Vol. 12, No. 1, 1970, pp. 9–20.

[9] Houdkova, S., Kasparova, M., and Zahalka, F., "The Influence of Spraying Angle on Properties of HVOF Sprayed Hardmetal Coatings," *Journal of Thermal Spray Technology*, Vol. 19, No. 5, 2010, pp. 893–901.

[10] Ilavsky, J., Allen, A. J., Long, G. G., and Krueger, S., "Influence of Spray Angle on the Pore and Crack Microstructure of Plasma-Sprayed Deposits," *Journal of the American Ceramic Society*, Vol. 80, No. 3, 1996, pp. 733–742.

[11] Kanouff, M. P., Neiser, R. A., and Roemer, T. J., "Surface Roughness of Thermal Spray Coatings Made with Off-Normal Spray Angles," *Journal of Thermal Spray Technology*, Vol. 7, No. 2, 1998, pp. 219–228.

[12] Montavon, G., Sampath, S., Berndt, C. C., Herman, H., and Coddet, C., "Effects of the Spray Angle on Splat Morphology During Thermal Spraying," *Surface and Coatings Technology*, Vol. 91, 1997, pp. 107–115.

[13] Smith, M. F., Neiser, R. A., and Dykhuizen, R. C., "An Investigation of the Effects of Droplet Impact Angle in Thermal Spray Deposition," *Proceedings of the 7th National Thermal Spray Conference*, 1997, pp. 603–608.

[14] Strock, E., Ruggiero, P., and Reynolds, D., "The Effect of Off-Angle Spraying on the Structure and Properties of HVOF WC/CoCr Coatings," *International Thermal Spray Conference*, 2001, pp. 671–676.

[15] Tillman, W., Vogli, E., and Krebs, B., "Influence of the Spray Angle on the Characteristics of Atmospheric Plasma Sprayed Hard Material Based Coatings," *Journal of Thermal Spray Technology*, Vol. 17, No. 5-6, 2008, pp. 948–955.

[16] Ang, C. B., Devasenapathi, A., Ng, H. W., Yu, S. C. M., and Lam, Y. C., "A Proposed Process Control Chart for DC Plasma Spraying Process, Part II Experimental Verification for Spraying Alumina," *Plasma Chemistry and Plasma Processing*, Vol. 21, No. 3, 2001, pp. 401–420.

[17] An, L. T. and Gao, Y., "Effect of Powder Injection Location on Ceramic Coatings Properties When Using Plasma Spray," *Journal of Thermal Spray Technology*, Vol. 16, No. 5-6, 2007, pp. 967–973.

[18] Vardelle, M., Vardelle, A., Fauchais, P., Li, K. I., Dussoubs, B., and Themelis, N. J., "Controlling Particle Injection in Plasma Spraying," *Journal of Thermal Spray Technology*, Vol. 10, No. 2, 2001, pp. 267–284.

[19] Xiong, H. B., Zheng, L. L., Sampath, S., Williamson, R. L., and Fincke, J. R., "Three-Dimensional Simulation of Plasma Spray: Effects of Carrier Gas Flow and Particle Injection on Plasma Jet and Entrained Particle Behavior," *International Journal of Heat and Mass Transfer*, Vol. 47, 2004, pp. 5189–5200.

[20] Li, H. P. and Chen, X., "Three-Dimensional Simulation of a Plasma Jet with Transverse Particle and Carrier Gas Injection," *Thin Solid Films*, Vol. 390, 2001, pp. 175–180.

[21] Ramachandran, K. and Nishiyama, H., "Three-Dimensional Effects of Carrier Gas and Particle Injections on the Thermo-Fluid Fields of Plasma Jets," *Journal of Physics D: Applied Physics*, Vol. 35, 2002, pp. 307–317.

[22] Kitahara, S. and Hasui, A., "A Study of the Bonding Mechanism of Sprayed Coatings," *Journal of Vacuum Science and Technology*, Vol. 11, No. 4, 1974, pp. 747–753.

[23] Wang, S. P., Wang, G. X., and Matthys, E. F., "Deposition of a Molten Layer of High Melting Point Material: Substrate Melting and Resolidification," *Materials Science and Engineering*, Vol. A262, 1999, pp. 25–32.

[24] Li, L., Wang, X. Y., Wei, G., Vaidya, A., Zhang, H., and Sampath, S., "Substrate Melting During Thermal Spray Splat Quenching," *Thin Solid Films*, Vol. 468, 2004, pp. 113–119.

[25] "SprayWatch," *http://www.oseir.com*.

[26] Mabey, K., Smith, B. L., Whichard, G., and McKechnie, T., "Coanda-assisted Spray Manipulation (CSM) Collar for a Commercial Plasma Spray Gun," *Journal of Thermal Spray Technology*, 2011.

# Appendix

## A.1 Vector Angle Data

Table A.1: Vector angle data for the $a/D = 2.0$ case with slot size of 15% circumference and a Reynolds number of 45300.

| $J^*$ | $\theta_{avg}$ | Skewness | Kurtosis | Standard Deviation |
|---|---|---|---|---|
| 0.01 | 2.3678 | 0.5094 | 3.3047 | 2.2438 |
| 0.0178 | 3.1985 | -0.2998 | 2.7285 | 2.4417 |
| 0.0274 | 5.6917 | 0.1197 | 3.0891 | 2.1958 |
| 0.0392 | 6.0701 | -0.00027 | 3.2637 | 2.1246 |
| 0.0530 | 7.0490 | 0.0609 | 2.8517 | 1.9425 |
| 0.0689 | 8.6504 | -0.0579 | 3.2407 | 1.9571 |
| 0.089 | 9.3262 | 0.2345 | 3.1920 | 1.8591 |

Table A.2: Vector angle data for the $a/D = 5.25$ case with slot size of 15% circumference and a Reynolds number of 45300.

| $J^*$ | $\theta_{avg}$ | Skewness | Kurtosis | Standard Deviation |
|---|---|---|---|---|
| 0.01 | 2.3080 | -0.0598 | 3.3939 | 2.9658 |
| 0.0178 | 3.1280 | 0.0167 | 3.1178 | 3.1956 |
| 0.0274 | 4.1113 | -0.0909 | 3.3846 | 3.6830 |
| 0.0392 | 9.0509 | -0.2698 | 3.0468 | 3.0599 |
| 0.0530 | 8.9414 | 0.0794 | 3.3401 | 3.5961 |
| 0.0689 | 8.4960 | 0.2332 | 3.9576 | 3.8725 |
| 0.089 | 8.8068 | 0.1628 | 3.4923 | 3.8525 |

Table A.3: Vector angle data for the $a/D = 2.0$ case with slot size of 30% circumference and a Reynolds number of 45300.

| $J^*$ | $\theta_{avg}$ | Skewness | Kurtosis | Standard Deviation |
|---|---|---|---|---|
| 0.01 | 0.2642 | -0.2197 | 3.1746 | 1.7220 |
| 0.01 | -0.5697 | -0.0321 | 3.0142 | 1.9698 |
| 0.0178 | -0.8930 | -0.1073 | 3.2752 | 2.0865 |
| 0.0178 | -1.2952 | -0.1162 | 2.6960 | 2.3997 |
| 0.0274 | -0.7945 | -0.3144 | 3.5410 | 2.2802 |
| 0.0274 | -0.6926 | -0.0772 | 3.0435 | 2.4055 |
| 0.0392 | -0.4511 | -0.1050 | 2.8490 | 2.5180 |
| 0.0392 | -0.6361 | -0.0088 | 3.0847 | 2.2211 |
| 0.0530 | 2.4569 | 0.1068 | 3.0603 | 2.3143 |
| 0.0530 | 1.1705 | -0.1365 | 2.5764 | 2.3086 |
| 0.0689 | 6.4949 | -0.1823 | 2.0365 | 3.9532 |
| 0.0689 | 4.3284 | 0.0360 | 2.6976 | 2.4745 |
| 0.089 | 5.9058 | 0.1158 | 2.6512 | 3.0600 |
| 0.089 | 6.5867 | -0.0211 | 2.7040 | 3.2472 |

Table A.4: Vector angle data for the $a/D = 5.25$ case with slot size of 30% circumference and and a Reynolds number of 45300.

| $J^*$ | $\theta_{avg}$ | Skewness | Kurtosis | Standard Deviation |
|---|---|---|---|---|
| 0.01 | 6.1107 | 0.0147 | 2.7472 | 2.4761 |
| 0.0178 | 7.7876 | -0.0731 | 3.2200 | 2.3779 |
| 0.0274 | 9.0229 | -0.1196 | 2.7669 | 2.5878 |
| 0.0392 | 10.5141 | -0.1437 | 3.5150 | 2.9214 |
| 0.0530 | 13.5023 | -0.0855 | 3.2332 | 2.5527 |
| 0.0689 | 13.5023 | -0.2074 | 3.1639 | 2.7746 |
| 0.089 | 9.8560 | -0.1837 | 3.0149 | 3.8233 |

Table A.5: Vector angle data for the $a/D = 2.0$ case with slot size of 30% circumference and a Reynolds number of 22600.

| $J^*$ | $\theta_{avg}$ | Skewness | Kurtosis | Standard Deviation |
|---|---|---|---|---|
| 0.01 | 0.6566 | -0.3469 | 2.9585 | 2.0377 |
| 0.0178 | -0.3288 | -0.3067 | 3.4141 | 2.4489 |
| 0.0274 | -0.6642 | -0.3120 | 2.8799 | 2.6158 |
| 0.0392 | -1.1305 | -0.1783 | 2.6460 | 2.9396 |
| 0.0530 | 0.1653 | -0.0118 | 2.6987 | 3.0253 |
| 0.0689 | 3.7383 | 0.0319 | 2.7969 | 3.2420 |
| 0.089 | 9.8148 | -0.1400 | 2.9514 | 2.6402 |

Table A.6: Vector angle data for the $a/D = 2.0$ case with slot size of 30% circumference and a Reynolds number of 67900.

| $J^*$ | $\theta_{avg}$ | Skewness | Kurtosis | Standard Deviation |
|---|---|---|---|---|
| 0.01 | 3.8426 | 0.2916 | 3.0135 | 2.8714 |
| 0.0178 | 3.4225 | 0.3063 | 3.2897 | 3.4381 |
| 0.0274 | 2.8005 | 0.2812 | 3.1969 | 3.8408 |
| 0.0392 | 7.7241 | 0.3472 | 2.8140 | 4.4900 |
| 0.0530 | 9.2649 | 0.4004 | 2.7319 | 4.4804 |
| 0.0689 | 9.4390 | 1.0896 | 4.0020 | 3.8272 |
| 0.089 | 7.8949 | 1.4900 | 8.2181 | 3.6355 |

## A.2 Design Drawings

Drawings of the two plasma spray devices are shown below.

| REVISION HISTORY | | | |
|---|---|---|---|
| REV | DESCRIPTION | DATE | APPROVED |
| | | | |

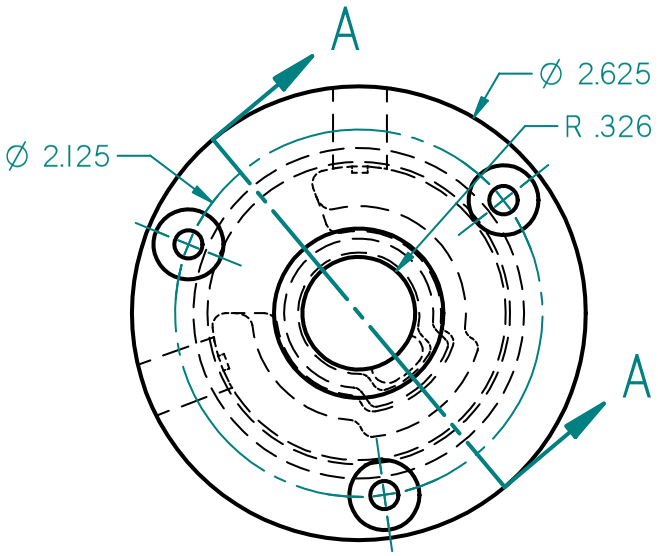


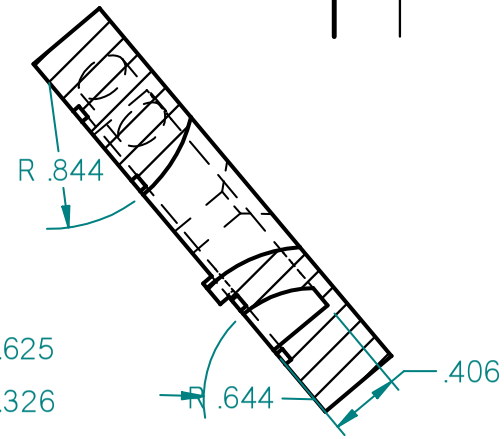


SECTION A-A

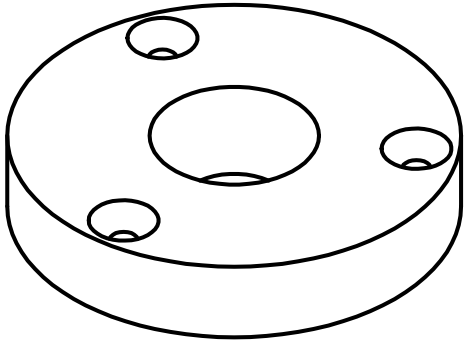

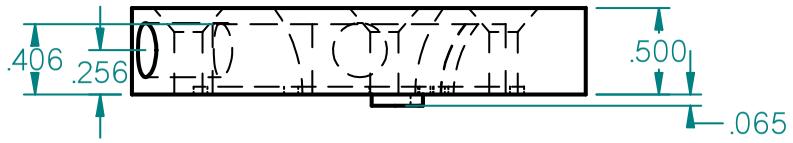


| | NAME | DATE |
|---|---|---|
| DRAWN | K Mabey | 03/25/11 |
| CHECKED | | |
| ENG APPR | | |
| MGR APPR | | |

UNLESS OTHERWISE SPECIFIED
DIMENSIONS ARE IN INCHES
ANGLES ±X.X°
2 PL ±X.XX 3 PL ±X.XXX

Solid Edge

TITLE
Small Plasma Spray Device - Top

| SIZE | DWG NO | REV |
|---|---|---|
| A | | |

FILE NAME: plasma_modify_collar_small_angl

| SCALE: | WEIGHT: | SHEET 1 OF 2 |
|---|---|---|

| REVISION HISTORY | | | |
|---|---|---|---|
| REV | DESCRIPTION | DATE | APPROVED |
| | | | |

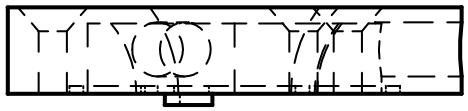

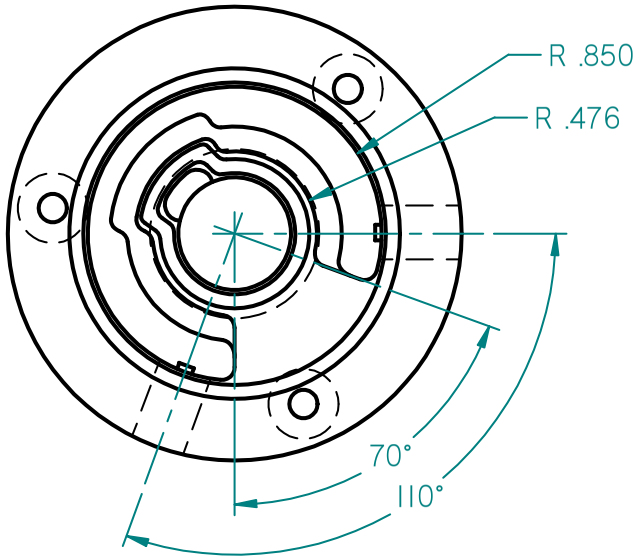


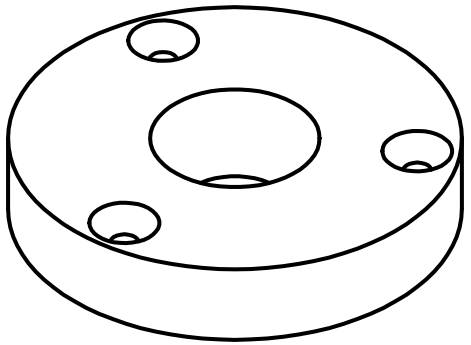

| | NAME | DATE |
|---|---|---|
| DRAWN | K Mabey | 03/25/11 |
| CHECKED | | |
| ENG APPR | | |
| MGR APPR | | |

UNLESS OTHERWISE SPECIFIED
DIMENSIONS ARE IN INCHES
ANGLES ±X.X°
2 PL ±X.XX 3 PL ±X.XXX

Solid Edge

TITLE
Small Plasma Spray Device - Top

| SIZE | DWG NO | REV |
|---|---|---|
| A | | |

FILE NAME: plasma_modify_collar_small_angl

| SCALE: | WEIGHT: | SHEET 2 OF 2 |
|---|---|---|

| REVISION HISTORY | | | |
|---|---|---|---|
| REV | DESCRIPTION | DATE | APPROVED |
| | | | |

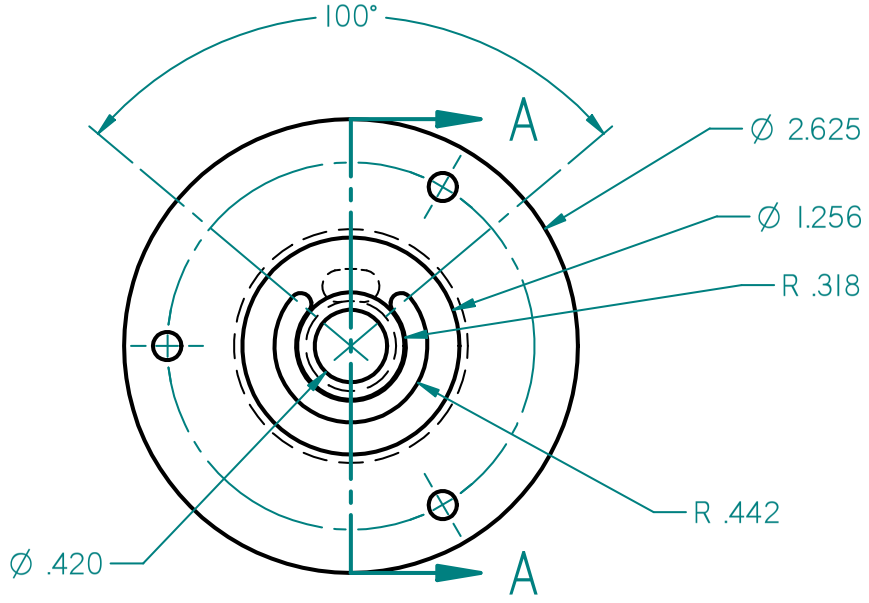


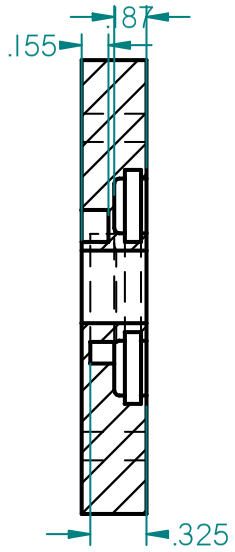


SECTION A-A

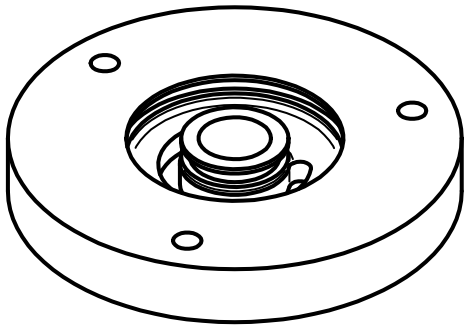

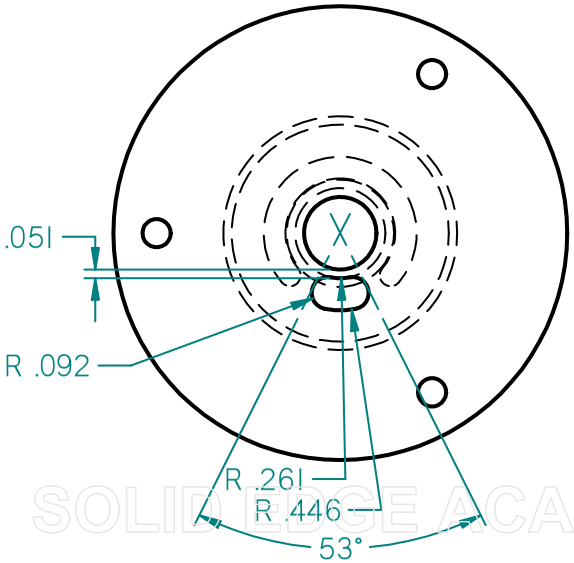


| | NAME | DATE |
|---|---|---|
| DRAWN | K Mabey | 03/25/11 |
| CHECKED | | |
| ENG APPR | | |
| MGR APPR | | |

UNLESS OTHERWISE SPECIFIED
DIMENSIONS ARE IN INCHES
ANGLES ±X.X°
2 PL ±X.XX 3 PL ±X.XXX

Solid Edge

TITLE
Small Plasma Spray Device - Bottom

| SIZE | DWG NO | REV |
|---|---|---|
| A | | |

FILE NAME: plasma_modify_bottom_small_an

| SCALE: | WEIGHT: | SHEET 1 OF 1 |
|---|---|---|

| REVISION HISTORY | | | |
|---|---|---|---|
| REV | DESCRIPTION | DATE | APPROVED |
| | | | |

# SECTION A-A

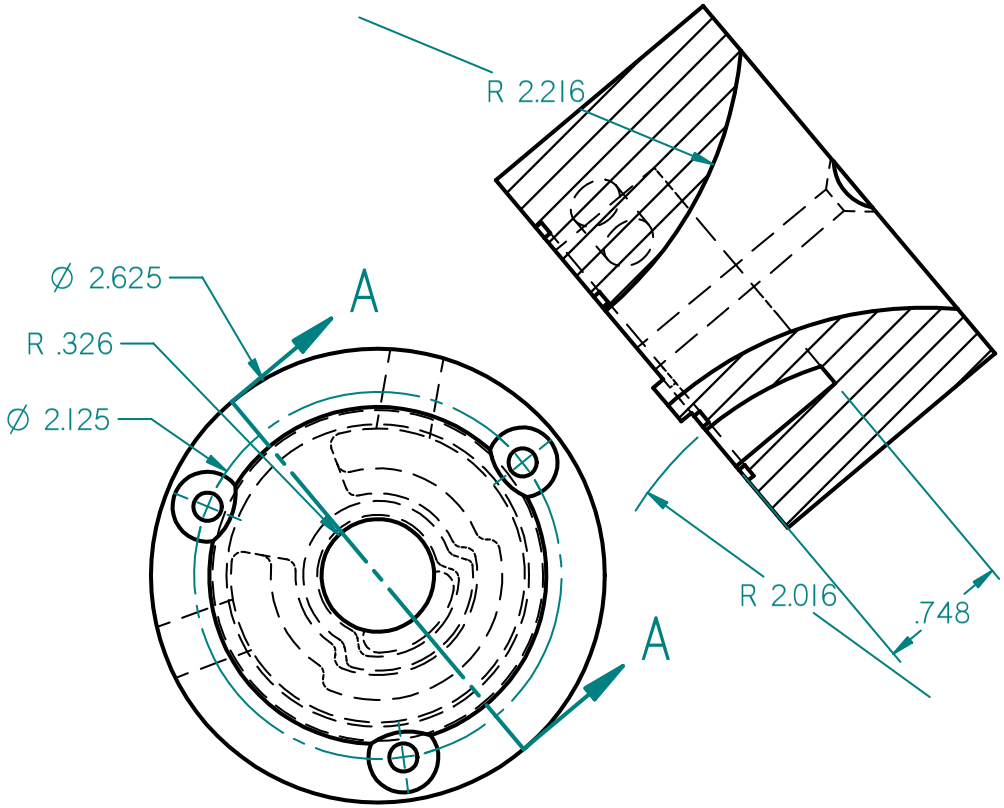


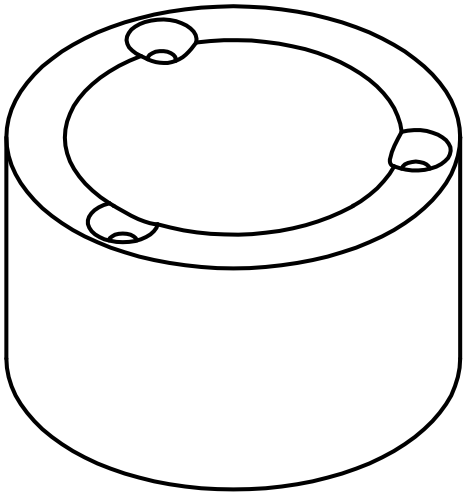

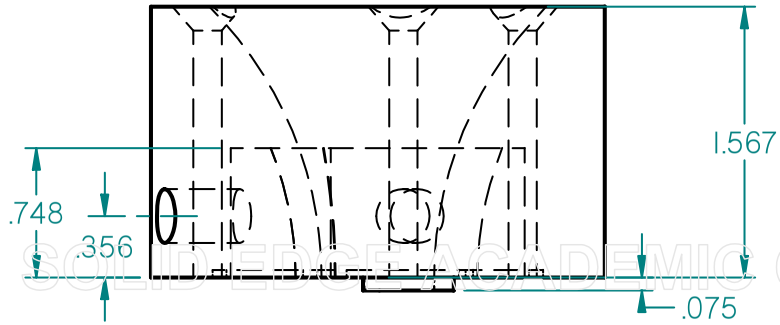


| | NAME | DATE |
|---|---|---|
| DRAWN | K Mabey | 03/25/11 |
| CHECKED | | |
| ENG APPR | | |
| MGR APPR | | |

UNLESS OTHERWISE SPECIFIED
DIMENSIONS ARE IN INCHES
ANGLES ±X.X°
2 PL ±X.XX 3 PL ±X.XXX

Solid Edge

TITLE
Large Plasma Spray Device - Top

| SIZE | DWG NO | REV |
|---|---|---|
| A | | |

FILE NAME: plasma_modify_collar_large_angle

| SCALE: | WEIGHT: | SHEET 1 OF 2 |
|---|---|---|

| REVISION HISTORY | | | |
|---|---|---|---|
| REV | DESCRIPTION | DATE | APPROVED |
| | | | |

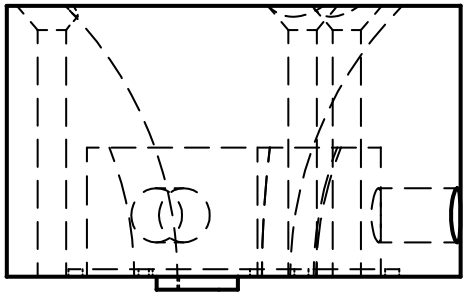

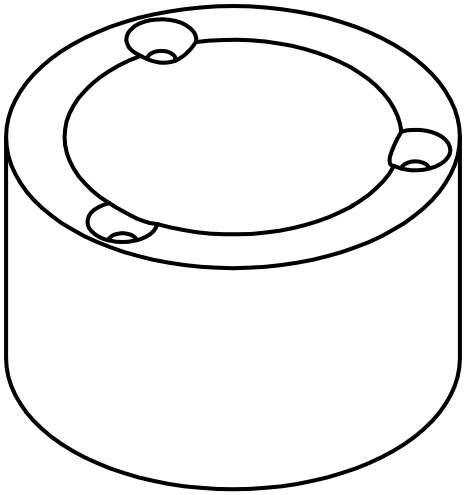

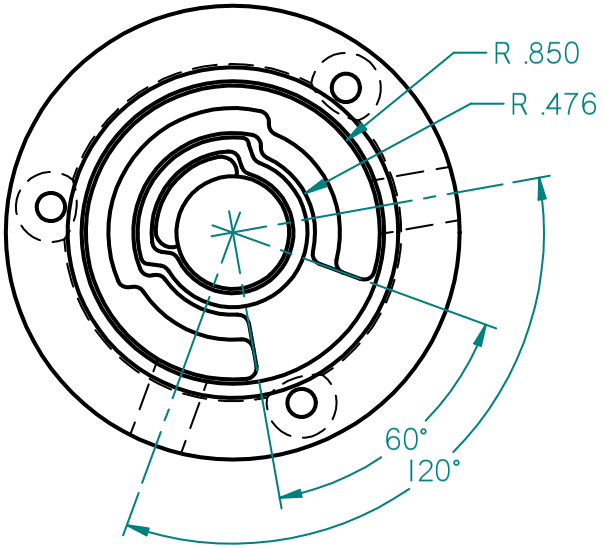


| | NAME | DATE |
|---|---|---|
| DRAWN | K Mabey | 03/25/11 |
| CHECKED | | |
| ENG APPR | | |
| MGR APPR | | |

UNLESS OTHERWISE SPECIFIED
DIMENSIONS ARE IN INCHES
ANGLES ±X.X°
2 PL ±X.XX 3 PL ±X.XXX

Solid Edge

TITLE
Large Plasma Spray Device - Top

| SIZE | DWG NO | REV |
|---|---|---|
| A | | |

FILE NAME: plasma_modify_collar_large_angle

| SCALE: | WEIGHT: | SHEET 2 OF 2 |
|---|---|---|

| REVISION HISTORY | | | |
|---|---|---|---|
| REV | DESCRIPTION | DATE | APPROVED |
| | | | |

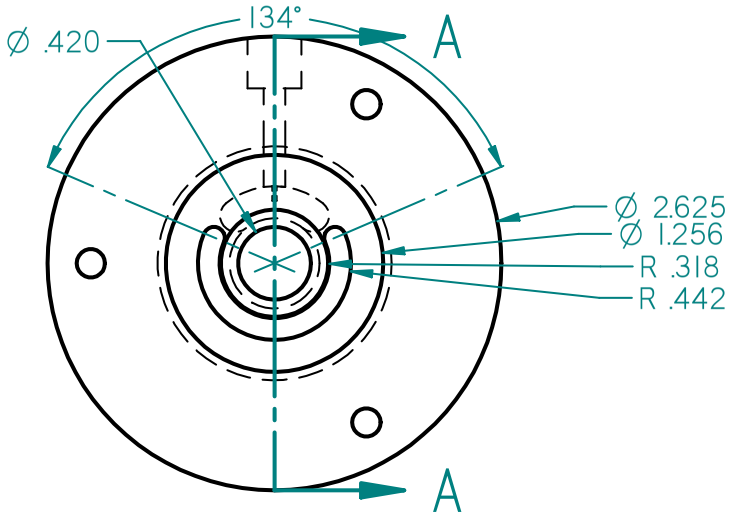


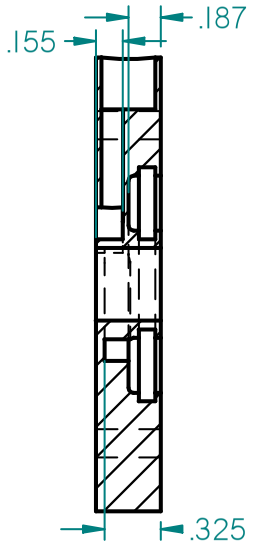


SECTION A-A

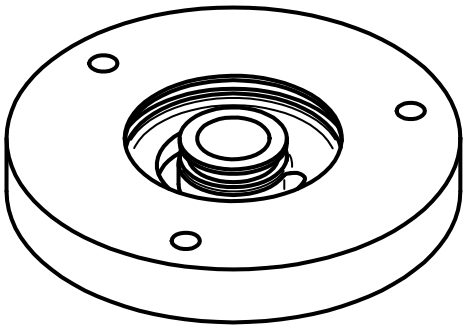

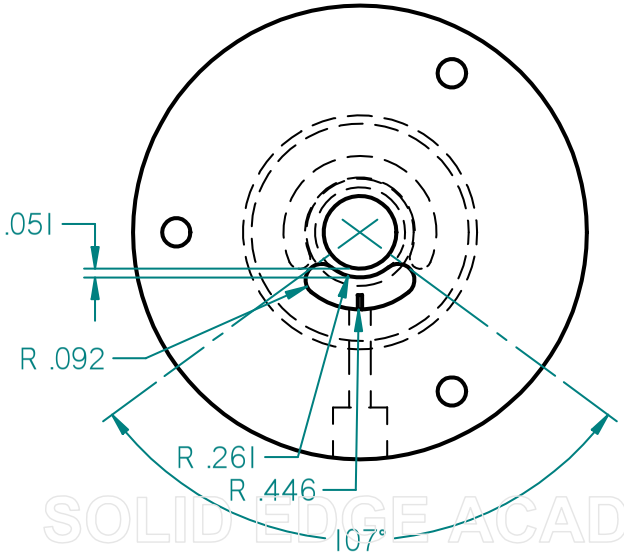




| | NAME | DATE |
|---|---|---|
| DRAWN | K Mabey | 03/25/11 |
| CHECKED | | |
| ENG APPR | | |
| MGR APPR | | |

UNLESS OTHERWISE SPECIFIED
DIMENSIONS ARE IN INCHES
ANGLES ±X.X°
2 PL ±X.XX 3 PL ±X.XXX

Solid Edge

TITLE
Large Plasma Spray Device - Bottom

| SIZE | DWG NO | REV |
|---|---|---|
| A | | |

FILE NAME: plasma_modify_bottom_large_ang

| SCALE: | WEIGHT: | SHEET 1 OF 1 |
|---|---|---|

## A.3 Matlab Code

### A.3.1 Rotation Study Code

The following code computes the center of velocity for all 1024 velocity fields for each rotation study case, the mean radius of the circle traced out by rotating the vectored jet for every circumferential location, and the RMS of the data about that mean at each circumferential location. It also computes a mean circle for all data points.

```
%This code reads in Davis .vc7 vector fields and computes a center of
%velocity similar to the computation of a center of mass

%A Clean Matlab is a Happy Matlab
clc, clear all, close all



%% Read the average files and find thier center of velocity
%Preallocate
mean_loc_bar(1:50,1:2) = NaN;

%Point to the location of the images (selecet any file within the folder to
%read from).

f = 'B00001_Avg V.VC7';
[s,t] = uigetfile;
for k = 1:50
    %File name of the .VC7 vector file (following the default B00001.VC7
    %naming scheme).
    num = sprintf('%02g',k);
    p = [t,'average_',num, '\'];
```

```
    %Open the file with readimx
    A = readimx([p,f]);

    if A.ScaleI(1) == 0
        A.ScaleI(1) = 13.8525;
    end

% ** This section of code is from showimx.m from Lavision **



    %Check image type and data format
    nx = size(A.Data,1);
    nz = A.Nz;
    ny = A.Ny;
    %set data range
    drng_x = 1:nx;
    drng_y = 1:ny;
    drng_z = 1:nz;
    %initialize left handside values
    lhs1 = (drng_x-0.5)*A.Grid*A.ScaleX(1)+A.ScaleX(2); % x-range
    lhs2 = (drng_y-0.5)*A.Grid*A.ScaleY(1)+A.ScaleY(2); % y-range
    % Calculate vector position and components
    if A.IType<=0, % grayvalue image format
    % Calculate frame range
    if frame>0 & frame<A.Nf,
        drng_y = drng_y + frame*ny;
```

```
    end
    lhs3 = A.Data(:,drng_y)';
    % Display image
    imagesc(lhs1,lhs2,lhs3);
elseif A.IType==2, % simple 2D vector format: (vx,vy)
    % Calculate vector position and components
    [lhs1,lhs2] = ndgrid(lhs1,lhs2);
    lhs3 = A.Data(:,drng_y   )*A.ScaleI(1)+A.ScaleI(2);
    lhs4 = A.Data(:,drng_y+ny)*A.ScaleI(1)+A.ScaleI(2);
    if A.ScaleY(1)<0.0,
        lhs4 = -lhs4;
    end

elseif (A.IType==3 | A.IType==1) , % normal 2D vector format + peak: sel+4*(vx,vy) (+peak)
    % Calculate vector position and components
    [lhs1,lhs2] = ndgrid(lhs1,lhs2);
    lhs3 = lhs1*0;
    lhs4 = lhs2*0;
    % Get choice
    lhs5 = A.Data(:,drng_y);
    % Build best vectors from choice field
    for i = 0:5,
        mask=(lhs5==(i+1));
        if (i<4) % get best vectors
            dat = A.Data(:,drng_y+(2*i+1)*ny);
            lhs3(mask) = dat(mask);
            dat = A.Data(:,drng_y+(2*i+2)*ny);
            lhs4(mask) = dat(mask);
```

```
        else    % get interpolated vectors
            dat = A.Data(:,drng_y+7*ny);
            lhs3(mask) = dat(mask);
            dat = A.Data(:,drng_y+8*ny);
            lhs4(mask) = dat(mask);
        end
    end
    lhs3 = lhs3*A.ScaleI(1)+A.ScaleI(2);
    lhs4 = lhs4*A.ScaleI(1)+A.ScaleI(2);
    %Display vector field
    if A.ScaleY(1)<0.0,
        lhs4 = -lhs4;
    end

elseif A.IType==4,
    % Calculate vector position and components
    lhs3 = (drng_z-0.5)*A.Grid*A.ScaleY(1)+A.ScaleY(2);
    lhs4 = A.Data(:,drng_y     )*A.ScaleI(1)+A.ScaleI(2);
    lhs5 = A.Data(:,drng_y+  ny)*A.ScaleI(1)+A.ScaleI(2);
    lhs6 = A.Data(:,drng_y+2*ny)*A.ScaleI(1)+A.ScaleI(2);
    [lhs1,lhs2,lhs3] = ndgrid(lhs1,lhs2,lhs3);
elseif A.IType==5,
    % Calculate vector position and components
    lhs3 = (drng_z-0.5)*A.Grid*A.ScaleZ(1)+A.ScaleZ(2);
    lhs4 = zeros([nx ny nz]);
    lhs5 = lhs4;
    lhs6 = lhs4;
    for iz=1:nz,
```

```
px = zeros([nx ny]);
py = zeros([nx ny]);
pz = zeros([nx ny]);
prange = drng_y + ((iz-1)*14*ny);
% Build best vectors from best choice field
lhs7 = A.Data(:,prange);
for i = 0:5,
    if (i<4) % get best vectors
        mask = (lhs7==(i+1));
        dat = A.Data(:,prange+(3*i+1)*ny);
        px(mask) = dat(mask);
        dat = A.Data(:,prange+(3*i+2)*ny);
        py(mask) = dat(mask);
        dat = A.Data(:,prange+(3*i+3)*ny);
        pz(mask)=dat(mask);
    else    % get interpolated vectors
        mask = (lhs7==(i+1));
        dat = A.Data(:,prange+10*ny);
        px(mask) = dat(mask);
        dat = A.Data(:,prange+11*ny);
        py(mask) = dat(mask);
        dat = A.Data(:,prange+12*ny);
        pz(mask) = dat(mask);
    end
end
lhs4(:,:,iz)=px;
lhs5(:,:,iz)=py;
lhs6(:,:,iz)=pz;
```

```
    end
    [lhs1,lhs2,lhs3] = ndgrid(lhs1,lhs2,lhs3);
    lhs4 = lhs4*A.ScaleI(1)+A.ScaleI(2);
    lhs5 = lhs5*A.ScaleI(1)+A.ScaleI(2);
    lhs6 = lhs6*A.ScaleI(1)+A.ScaleI(2);
end

    %scale the davis coordinate system by the diameter of the jet (.5in)
    lhs1 = lhs1/12.7;
    lhs2 = lhs2/12.7;

    %Compute the 'center of velocity'
    m = 0;
    xm = 0;
    ym = 0;
    %compute the magnitue of each velocity vector
    dimensions = size(lhs6);
    mean_mag(:,:) = sqrt(lhs4.^2+lhs5.^2+lhs6.^2);

    % Find the bulk flow rate
    mean_sum_vel = 0;
    c = 0;
    mean_half_max = (1/3)*max(max(mean_mag));
    for n = 1:dimensions(1)
        for o = 1:dimensions(2)
            if mean_mag(n,o) > mean_half_max
            mean_sum_vel = mean_sum_vel + mean_mag(n,o);
            c = c+1;
```

```
            end
        end
    end
    mean_bulk_vel = mean_sum_vel/c;
    mean_threshold = mean_bulk_vel/2.;
    %compute the sums used in the centroid calculation
    for j = 1:ny
        for i = 1:nx
            if mean_mag(i,j) <= mean_threshold
                mean_mag(i,j) = 0;
            end
            m = m + mean_mag(i,j);
            xm = xm + mean_mag(i,j)*lhs1(i,j);
            ym = ym + mean_mag(i,j)*lhs2(i,j);
        end
    end

    %compute the centroid
    mean_loc_bar(k,1) = xm/m;
    mean_loc_bar(k,2) = ym/m;
    if abs(mean_loc_bar(k,1)) > 75
        mean_loc_bar(k,1) = 0;
    end

    if abs(mean_loc_bar(k,2)) > 75
        mean_loc_bar(k,2) = 0;
    end
end
```

```
%% Read in the actual vector fields and find thier center of velocity
%Number of Vector fields to be read
npics = 1024;   %       <-----------  CHAMGE ME!
n(1:npics) = 0;
%Preallocate
loc_bar(1:npics,1:2) = NaN;

for k = 1:npics
    %File name of the .VC7 vector file (following the default B00001.VC7
    %naming scheme).
    num = sprintf('%05g',k);
    f = ['B',num,'.VC7'];

    %Open the file with readimx
    A = readimx([t,f]);

    if A.ScaleI(1) == 0
        A.ScaleI(1) = 13.8525;
    end

% ** This section of code is from showimx.m from Lavision **



    %Check image type and data format
    nx = size(A.Data,1);
    nz = A.Nz;
```

```
    ny = A.Ny;
    %set data range
    drng_x = 1:nx;
    drng_y = 1:ny;
    drng_z = 1:nz;
    %initialize left handside values
    lhs1 = (drng_x-0.5)*A.Grid*A.ScaleX(1)+A.ScaleX(2); % x-range
    lhs2 = (drng_y-0.5)*A.Grid*A.ScaleY(1)+A.ScaleY(2); % y-range
    % Calculate vector position and components
    if A.IType<=0, % grayvalue image format
    % Calculate frame range
    if frame>0 & frame<A.Nf,
        drng_y = drng_y + frame*ny;
    end
    lhs3 = A.Data(:,drng_y)';
    % Display image
    imagesc(lhs1,lhs2,lhs3);
elseif A.IType==2, % simple 2D vector format: (vx,vy)
    % Calculate vector position and components
    [lhs1,lhs2] = ndgrid(lhs1,lhs2);
    lhs3 = A.Data(:,drng_y   )*A.ScaleI(1)+A.ScaleI(2);
    lhs4 = A.Data(:,drng_y+ny)*A.ScaleI(1)+A.ScaleI(2);
    if A.ScaleY(1)<0.0,
        lhs4 = -lhs4;
    end

elseif (A.IType==3 | A.IType==1) , % normal 2D vector format + peak: sel+4*(vx,vy) (+peak)
    % Calculate vector position and components
```

```
    [lhs1,lhs2] = ndgrid(lhs1,lhs2);
    lhs3 = lhs1*0;
    lhs4 = lhs2*0;
    % Get choice
    lhs5 = A.Data(:,drng_y);
    % Build best vectors from choice field
    for i = 0:5,
        mask=(lhs5==(i+1));
        if (i<4) % get best vectors
            dat = A.Data(:,drng_y+(2*i+1)*ny);
            lhs3(mask) = dat(mask);
            dat = A.Data(:,drng_y+(2*i+2)*ny);
            lhs4(mask) = dat(mask);
        else    % get interpolated vectors
            dat = A.Data(:,drng_y+7*ny);
            lhs3(mask) = dat(mask);
            dat = A.Data(:,drng_y+8*ny);
            lhs4(mask) = dat(mask);
        end
    end
    lhs3 = lhs3*A.ScaleI(1)+A.ScaleI(2);
    lhs4 = lhs4*A.ScaleI(1)+A.ScaleI(2);
    %Display vector field
    if A.ScaleY(1)<0.0,
        lhs4ab = -lhs4;
    end

elseif A.IType==4,
```

```
    % Calculate vector position and components
    lhs3 = (drng_z-0.5)*A.Grid*A.ScaleY(1)+A.ScaleY(2);
    lhs4 = A.Data(:,drng_y     )*A.ScaleI(1)+A.ScaleI(2);
    lhs5 = A.Data(:,drng_y+  ny)*A.ScaleI(1)+A.ScaleI(2);
    lhs6 = A.Data(:,drng_y+2*ny)*A.ScaleI(1)+A.ScaleI(2);
    [lhs1,lhs2,lhs3] = ndgrid(lhs1,lhs2,lhs3);
elseif A.IType==5,
    % Calculate vector position and components
    lhs3 = (drng_z-0.5)*A.Grid*A.ScaleZ(1)+A.ScaleZ(2);
    lhs4 = zeros([nx ny nz]);
    lhs5 = lhs4;
    lhs6 = lhs4;
    for iz=1:nz,
        px = zeros([nx ny]);
        py = zeros([nx ny]);
        pz = zeros([nx ny]);
        prange = drng_y + ((iz-1)*14*ny);
        % Build best vectors from best choice field
        lhs7 = A.Data(:,prange);
        for i = 0:5,
            if (i<4) % get best vectors
                mask = (lhs7==(i+1));
                dat = A.Data(:,prange+(3*i+1)*ny);
                px(mask) = dat(mask);
                dat = A.Data(:,prange+(3*i+2)*ny);
                py(mask) = dat(mask);
                dat = A.Data(:,prange+(3*i+3)*ny);
                pz(mask)=dat(mask);
```

```
            else    % get interpolated vectors
                mask = (lhs7==(i+1));
                dat = A.Data(:,prange+10*ny);
                px(mask) = dat(mask);
                dat = A.Data(:,prange+11*ny);
                py(mask) = dat(mask);
                dat = A.Data(:,prange+12*ny);
                pz(mask) = dat(mask);
            end
        end
        lhs4(:,:,iz)=px;
        lhs5(:,:,iz)=py;
        lhs6(:,:,iz)=pz;
    end
    [lhs1,lhs2,lhs3] = ndgrid(lhs1,lhs2,lhs3);
    lhs4 = lhs4*A.ScaleI(1)+A.ScaleI(2);
    lhs5 = lhs5*A.ScaleI(1)+A.ScaleI(2);
    lhs6 = lhs6*A.ScaleI(1)+A.ScaleI(2);
end

    %scale the davis coordinate system by the diameter of the jet (.5in)
    lhs1 = lhs1/12.7;
    lhs2 = lhs2/12.7;

    %Compute the 'center of velocity'
    m = 0;
    xm = 0;
    ym = 0;
```

```
%compute the magnitue of each velocity vector

mag(:,:) = sqrt(lhs4.^2+lhs5.^2+lhs6.^2);

% Find the bulk flow rate
sum_vel = 0;
c = 0;
half_max = (1/3)*max(max(mag));
for q = 1:dimensions(1)
    for o = 1:dimensions(2)
        if mag(q,o) > half_max
        sum_vel = sum_vel + mag(q,o);
        c = c+1;
        end
    end
end
bulk_vel(k) = sum_vel/c;
threshold = bulk_vel(k)/2.;
%compute the sums used in the centroid calculation
for j = 1:ny
    for i = 1:nx
        if mag(i,j) <= threshold
            mag(i,j) = 0;
        end
        m = m + mag(i,j);
        xm = xm + mag(i,j)*lhs1(i,j);
        ym = ym + mag(i,j)*lhs2(i,j);
    end
```

```
    end

    %compute the centroid
    loc_bar(k,1) = xm/m;
    loc_bar(k,2) = ym/m;
    if abs(loc_bar(k,1)) > 75
        loc_bar(k,1) = 0;
    end

    if abs(loc_bar(k,2)) > 75
        loc_bar(k,2) = 0;
    end

     maximumvel= max(max(lhs6));
 halfmaxvel = (max(max(lhs6)))/4.0;
   for i = 1:dimensions(1)
       for j = 1:dimensions(2)
           if (lhs6(i,j) >= halfmaxvel)
               n(k) = n(k)+1;
           end
       end
   end
end

%% calculate the RMS of the data set
x_center = mean(mean(loc_bar(:,1)));
y_center = mean(mean(loc_bar(:,2)));
```

```
loc_bar_new(:,1) = loc_bar(:,1)-x_center;
loc_bar_new(:,2) = loc_bar(:,2)-y_center;

mean_loc_bar_new(:,1) = mean_loc_bar(:,1)-x_center;
mean_loc_bar_new(:,2) = mean_loc_bar(:,2)-y_center;

% R = sqrt(mean_loc_bar_new(:,1).^2 + mean_loc_bar_new(:,2).^2);
 r = sqrt(loc_bar_new(:,1).^2 + loc_bar_new(:,2).^2);
% squared_sum(1:50) = 0.0;
% for i = 1:20
%     for j = 1:50
%         squared_sum(j) = squared_sum(j) + (R(j)-r((i-1)*50+j))^2;
%     end
% end
%
% rms = sqrt(squared_sum(:))/sqrt(20);
diameter(1:25) = NaN;
for j = 1:25
    diameter(j) = sqrt((mean_loc_bar_new(j,1)-mean_loc_bar_new(j+24,1))^2+(mean_loc_bar_ne
end
mean_diameter = mean(diameter);
mean_sum = 0;
s = 0;
for l=1:25
    if diameter(l)<1.1*mean_diameter || diameter(l)>0.9*mean_diameter
        mean_sum = mean_sum + diameter(l);
        s = s + 1;
    end
```

```
end

mean_radius = mean_sum/(s*2);
%need to put in circumferential position
for i = 1:50
    circ_position(i) = atan(mean_loc_bar_new(i,2)/mean_loc_bar_new(i,1));
    if mean_loc_bar_new(i,1)<0.0 && mean_loc_bar_new(i,2)>0.0
        circ_position_new(i) = -circ_position(i);
    elseif mean_loc_bar_new(i,1)>=0.0
        circ_position_new(i) = pi-circ_position(i);
    elseif mean_loc_bar_new(i,1)<0.0 && mean_loc_bar_new(i,2)<0.0
        circ_position_new(i) = 2*pi-circ_position(i);
    end
end
squared_sum_2(1:50) = 0.0;
for i=1:20
    for j=1:50
        squared_sum_2(j) = squared_sum_2(j)+(mean_radius-r((i-1)*50+j))^2;
    end
end

rms_2(:,2) = (sqrt(squared_sum_2(:))/sqrt(20))/mean_radius;
rms_2(1:50,1) = circ_position_new(1:50);

theta = transpose(0:360/50:352.8);
theta_2(1:1000) = NaN;
for k = 1:20
    theta_2((k-1)*50+1:(k)*50) = transpose(0:360/50:352.8);
```

```
end

r_mean(1:50) = mean_radius;

 x = [-mean_radius:mean_radius/100:mean_radius,-mean_radius:mean_radius/100:mean_radius];

 for in = 1:201
      y(in) = -sqrt(mean_radius^2-x(in)^2);
 end

 for in = 202:402
      y(in) = sqrt(mean_radius^2-x(in)^2);
 end

 x_new(1:801,1:2) = NaN;
 for in = 1:402
    x_new(in,1) = real(x(in));
    x_new(in,2) = real(y(in));
    x_new(in+402,1) = real(y(in));
    x_new(in+402,2) = real(x(in));
 end

 filename = input('Enter the file name you would like to output to: ', 's');
 for u = 1:npics
    num = sprintf('%05g',u);
    bottom = (floor(u/50))*50+1;
    f = [filename,num,'.txt'];
    %csvwrite(f,loc_bar_new(bottom:u,:))
```

```
end

x_circle(1:ab51) = (-mean_radius:(mean_radius/25):mean_radius);
y_circle(1:51) = sqrt(mean_radius^2-x_circle.^2);
y_circle(52:102) = -sqrt(mean_radius^2-x_circle.^2);
x_circle(52:102) = x_circle(51:-1:1);
circle(:,1) = x_circle;
circle(:,2) = y_circle;

csvwrite([filename,'avg.txt'],rms_2)

%% calculate the average area of the jet

dx=.0002078;
area(1:npics) = n(1:npics)*dx^2;
mean(area)
```

### A.3.2 Angle Calculation Code

The following code computes the vector angle for all 300 velocity fields for each small angle study case as well as the standard deviation, skewness, and kurtosis and produces a plot of the resulting distribution.

```
%This code reads in .dat (Tecplot) files and computes a weighted mean
%vector angle

%A Clean Matlab is a Happy Matlab
clc, clear all, close all
fclose('all');
```

```
%% Read the velocity feild files
%Number of Vector fields to be read
npics = 300;   %       <-----------  CHAMGE ME!
%Preallocate
theta_avg(1:npics) = 0.0;
for k = 1:npics
    %File name of the .dat vector file (following the default B00001.dat
    %naming scheme).
    num = sprintf('%03g',k);
    f = [num,'.txt'];
    i=2;
    fid = fopen(f);
    format = repmat('%f ', 1, i);
    A = textscan(fid, format);
    vel = cell2mat(A);
    [h,w] = size(vel);
    product(1:h) = 0.0;
    mag(1:h) = 0.0;
    theta(1:h) = 0.0;
    for j = 1:h
        mag(j) = sqrt(vel(j,1)^2+vel(j,2)^2);
        theta(j) = atan(vel(j,2)/vel(j,1));
        if (vel(j,1)==0)
            theta(j) = 0;
        end
    end
    avg_mag = mean(mag(:));
```

```
    for j = 1:h
        product(j) = mag(j)*theta(j);
    end
    theta_avg(k) = sum(product(:));
    theta_avg(k) = theta_avg(k)/(avg_mag*h);
    theta_avg(k) = 180*theta_avg(k)/pi;
end
figure(1);
x = -20:.5:10.0;
%hist(theta_avg,x);
hold on
total_avg_theta = mean(theta_avg);
st_dev_theta = std(theta_avg);
skew_ness = skewness(theta_avg);
kurt_osis = kurtosis(theta_avg);
```